CHALMERS
UNIVERSITY OF TECHNOLOGY

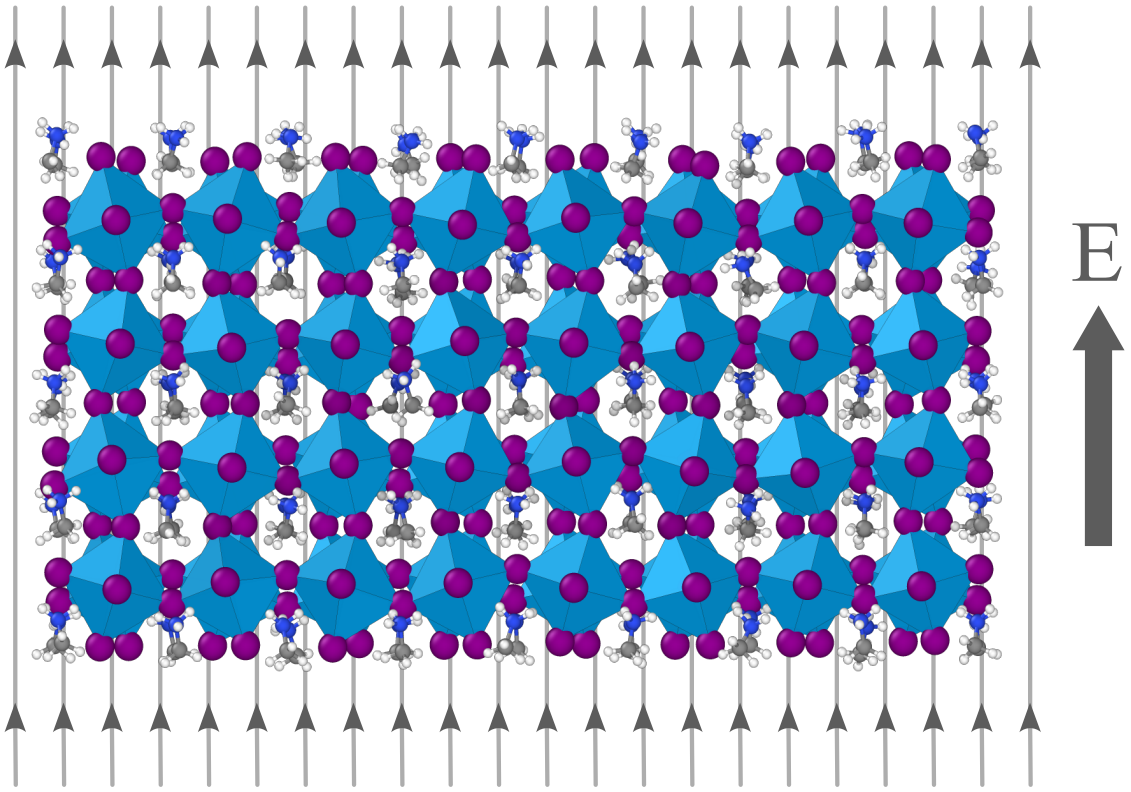

Electric field-induced phase transitions in the hybrid halide perovskite $MAPbI_3$

Atomistic insights into AC/DC-driven phase transitions via a charge-aware neuroevolution potential

Master's thesis in Physics

Ylva Liljegren

DEPARTMENT OF PHYSICS

CHALMERS UNIVERSITY OF TECHNOLOGY
Gothenburg, Sweden 2026
www.chalmers.se

Master's thesis 2026

Electric field-induced phase transitions in the hybrid halide perovskite $MAPbI_3$

Atomistic insights into AC/DC-driven phase transitions via a charge-aware neuroevolution potential

Ylva Liljegren

CHALMERS
UNIVERSITY OF TECHNOLOGY

Department of Physics
Division of Condensed Matter and Materials Theory
Computational Materials Research group
Chalmers University of Technology
Gothenburg, Sweden 2026

Electric field-induced phase transitions in the hybrid halide perovskite $MAPbI_3$
Atomistic insights into AC/DC-driven phase transitions via a charge-aware neuroevolution potential
Ylva Liljegren

Supervisor: Erik Fransson, Department of Physics
Examiner: Paul Erhart, Department of Physics

Master's Thesis 2026
Department of Physics
Division of Condensed Matter and Materials Theory
Computational Materials Research group
Chalmers University of Technology
SE-412 96 Gothenburg
Telephone +46 31 772 1000

Cover: $MAPbI_3$ perovskite structure under applied electric field.

Typeset in LaTeX
Printed by Chalmers Reproservice
Gothenburg, Sweden 2026

Electric field-induced phase transitions in the hybrid halide perovskite $MAPbI_3$
Atomistic insights into AC/DC-driven phase transitions via a charge-aware neuroevolution potential

Ylva Liljegren
Department of Physics
Chalmers University of Technology

Abstract

Hybrid halide perovskites have attracted significant attention due to their remarkable optoelectronic properties, which are sensitive to structural phase transitions. This work investigates electric field-induced phase transitions in methylammonium lead iodide ($MAPbI_3$), a prototypical hybrid halide perovskite, using molecular dynamics simulations with a charge-aware neuroevolution potential. The structural and dynamical response of $MAPbI_3$ to both static and oscillating electric fields is characterized across a range of temperatures, focusing on octahedral tilting, methylammonium (MA) cation orientations and vibrational properties.

Under static fields up to 0.1 V/Å, the orthorhombic-to-tetragonal phase transition temperature decreases while the tetragonal-to-cubic transition shifts to higher temperatures. Analysis of phonon mode projections indicates that electric fields induce a reorientation of the octahedral tilt pattern, with the dominant tilt axis preferentially oriented away from the field direction. A progressive alignment of MA molecular dipoles with increasing field strength is observed.

For oscillating fields, frequency-temperature phase diagrams constructed for two field strengths reveal a substantial suppression of transition temperatures across many frequencies, with pronounced resonant features at 1.3 THz and 2.4 THz. Vibrational analysis suggests that these resonances couple to infrared-active PbI_6 framework modes rather than direct MA dipole reorientation, providing insights into the intricate coupling between the inorganic lattice and organic cations that governs phase behavior under external fields.

Keywords: perovskites, phase transitions, electric fields, molecular dynamics, Born effective charges, neuroevolution potential

Acknowledgements

I would like to thank my examiner Paul Erhart for proposing this project and providing invaluable feedback throughout. I am equally grateful to my supervisor Erik Fransson for his exceptional support and insightful guidance. Together, their contributions have been instrumental in shaping this work.

I also appreciate the welcoming and collaborative environment at the Condensed Matter and Materials Theory Division, and thank everyone there for making this time productive and enjoyable.

Finally, I would like to thank my friends and family for their encouragement. A special thanks goes to Simon for enduring countless physics discussions along the way.

Ylva Liljegren, Gothenburg, June 2026

List of Acronyms

Below is the list of acronyms that have been used throughout this thesis listed in alphabetical order:

ACF	Autocorrelation function
BEC	Born effective charge
DFT	Density functional theory
DOS	Density of states
MA	Methylammonium
MD	Molecular dynamics
NEP	Neuroevolution potential
NPT	Isothermal-isobaric ensemble
NVE	Microcanonical ensemble
NVT	Canonical ensemble
PSD	Power spectral density
qNEP	Charge-aware neuroevolution potential

Contents

List of Figures

List of Tables

1
Introduction

1.1 Background

Hybrid halide perovskites are promising materials for photovoltaic applications due to their tunable bandgap, low-cost fabrication and power conversion efficiency surpassing 26% [1]. However, their sensitivity to environmental factors such as humidity and heat makes it challenging to achieve long-term structural stability [2]. Structural distortions can alter the electronic band structure, thereby impacting optoelectronic properties and photovoltaic performance [3].

$MAPbI_3$ is a prototypical hybrid halide perovskite where methylammonium (MA) cations occupy cavities within a lead iodide (Pb−I) octahedral framework [4]. The MA molecules possess a permanent electric dipole moment and rotational degrees of freedom, allowing them to reorient in response to their local environment [5]. This coupling between molecular orientation and framework distortions is a key mechanism governing the phase behavior and thus structural stability of $MAPbI_3$ [6, 7]. External electric fields provide a direct means to manipulate the orientation of MA dipoles [8] and thus probe their coupling to the inorganic lattice. In addition, oscillating electric fields can resonantly interact with lattice vibrational modes that affect macroscopic material properties [9]. Together, static and oscillating fields provide complementary routes to influence phase stability in hybrid perovskites.

This work employs molecular dynamics (MD) simulations with a charge-aware machine-learned interatomic potential to characterize the structural and dynamical response of $MAPbI_3$ to static and oscillating electric fields. By analyzing octahedral tilt patterns, MA orientations, vibrational spectra, and phase behavior across a range of field strengths and frequencies, this work provides atomistic insights into field-induced structural changes. It further highlights the interplay between MA rotational dynamics, lattice vibrations and the inorganic framework.

1.2 Aim

The aim of this project is to study the effect of external electric fields on phase transitions in hybrid halide perovskites, using $MAPbI_3$ as a representative system. Key quantities of interest include octahedral tilts, molecular cation orientations and vibrational properties, which are used to characterize field-induced phase behavior.

1.3 Limitations

The use of graphical processing units via the `GPUMD` package [10] enables MD simulations with machine-learned potentials at relatively low computational cost. However, these potentials are approximations built on density functional theory (DFT), and their accuracy is limited by the training set coverage. Although deviations are generally small, they can still matter.

MD simulations are inherently limited by system size and timescale. Simulations were restricted to systems of $\sim 10^4 - 10^5$ atoms and timescales of tens of nanoseconds, whereas experimental studies encompass $\sim 10^{23}$ atoms evolving over seconds to minutes. Additionally, the primary analysis is restricted to electric fields applied in a single crystallographic directions. The field strengths employed (up to $0.1\,\mathrm{V/Å}$) are substantially larger than typical experimental values, necessary to induce observable structural changes within the accessible simulation timescales.

2

Theory

2.1 Phonons

The following presentation of lattice dynamics follows standard treatments in condensed matter physics [11]. In a crystal, the atoms vibrate around their equilibrium positions. Due to interatomic forces, a displacement of one atom is coupled to the motion of its neighbors, leading to collective vibrational modes in which all atoms oscillate with well-defined frequencies. These collective excitations are described in terms of so-called phonons, which are quasiparticles associated with the normal modes of the lattice.

For small displacements $\boldsymbol{u}_l$ of atom l, the potential energy can be expanded to second order within the harmonic approximation

$$V = V_0 + \sum_{l\alpha} \left.\frac{\partial V}{\partial u_{l\alpha}}\right|_{\text{eq}} u_{l\alpha} + \frac{1}{2}\sum_{ll'}\sum_{\alpha\beta} \left.\frac{\partial^2 V}{\partial u_{l\alpha}\partial u_{l'\beta}}\right|_{\text{eq}} u_{l\alpha}u_{l'\beta} + \mathcal{O}(u^3), \tag{2.1}$$

where α denotes Cartesian indices. The second-order derivatives define the force constant matrix

$$\Phi_{l\alpha,l'\beta} = \left.\frac{\partial^2 V}{\partial u_{l\alpha}\partial u_{l'\beta}}\right|_{\text{eq}}. \tag{2.2}$$

Since the atoms are in equilibrium, the linear term in the expansion vanishes and the Hamiltonian can be written as

$$H = \frac{1}{2}\sum_{l\alpha} M_l \dot{u}_{l\alpha}^2 + \frac{1}{2}\sum_{ll'}\sum_{\alpha\beta} \Phi_{l\alpha,l'\beta}\, u_{l\alpha}u_{l'\beta}, \tag{2.3}$$

where the first term is the kinetic energy and M_l is the mass of atom l. The equation of motion becomes

$$M_l \ddot{u}_{l\alpha} = -\sum_{l'\beta} \Phi_{l\alpha,l'\beta}\, u_{l'\beta}. \tag{2.4}$$

The relevant solutions are in the form of plane waves

$$u_{l\alpha,\nu}(t) = \frac{1}{\sqrt{M_l}}\epsilon_{l\alpha,\nu}(\boldsymbol{q})e^{i(\boldsymbol{q}\cdot\boldsymbol{R}_l - \omega_\nu(\boldsymbol{q})t)}, \tag{2.5}$$

where $\epsilon_{l\alpha,\nu}(\boldsymbol{q})$ describes the polarization of the vibration and ν labels the phonon branch. Substituting this into the equation of motion gives the following eigenvalue equation

$$\sum_{l'\beta} D_{l\alpha,l'\beta}(\boldsymbol{q})\epsilon_{l'\beta,\nu}(\boldsymbol{q}) = \omega_\nu^2(\boldsymbol{q})\epsilon_{l\alpha,\nu}(\boldsymbol{q}), \tag{2.6}$$

with the dynamical matrix defined as

$$D_{l\alpha,l'\beta}(\boldsymbol{q}) = \frac{1}{\sqrt{M_l M_{l'}}} \Phi_{l\alpha,l'\beta} e^{i\boldsymbol{q}\cdot(\boldsymbol{R}_l - \boldsymbol{R}_{l'})}. \tag{2.7}$$

The eigenvectors $\epsilon_{l\alpha,\nu}$ and eigenvalues $\omega_\nu^2(\boldsymbol{q})$ in Equation (2.6) represent the phonon modes and their corresponding (squared) vibrational frequencies. For every crystal momentum vector $\boldsymbol{q}$, there are $3n$ eigenvalues, where n is the number of atoms in the unit cell. Translational invariance of the total energy leads to the acoustic sum rule, ensuring that three modes satisfy $\omega_\nu(\mathbf{q} = 0) = 0$. These correspond to the acoustic phonon modes. The remaining $3n - 3$ modes have finite frequencies at $\boldsymbol{q} = 0$ and are referred to as optical modes. Positive eigenvalues $\omega_\nu^2(\boldsymbol{q}) > 0$ indicate stable oscillatory modes, while negative eigenvalues $\omega_\nu^2(\boldsymbol{q}) < 0$ correspond to imaginary frequencies associated with structural instabilities of the assumed equilibrium configuration.

Because of the periodicity of the crystal lattice, the dynamical matrix satisfies

$$\boldsymbol{D}(\boldsymbol{q} + \boldsymbol{G}) = \boldsymbol{D}(\boldsymbol{q}), \tag{2.8}$$

where $\boldsymbol{G}$ is any lattice vector in the reciprocal space. Therefore, it is sufficient to only consider the first Brillouin zone.

2.2 Born effective charges and dielectric response

The macroscopic polarization $\mathbf{P}$ describes the electric dipole moment per unit volume Ω and includes both ionic and electronic contributions. The Born effective charge (BEC) tensor $Z^*_{i,\alpha\beta}$ relates the induced polarization to atomic displacements in different Cartesian directions as

$$Z^*_{i,\alpha\beta} = \Omega \frac{\partial P_\alpha}{\partial u_{i,\beta}}, \tag{2.9}$$

where α denotes the polarization direction and β the displacement direction of atom i. Equivalently, the BEC tensor can be interpreted as the change in force on atom i induced by an external electric field,

$$Z^*_{i,\alpha\beta} = \frac{\partial F_{i,\beta}}{\partial E_\alpha}. \tag{2.10}$$

This equivalence follows from the fact that both polarization and force can be expressed as derivatives of the total energy U with respect to atomic displacements and electric field, respectively [12], i.e.

$$P_\alpha = -\frac{1}{\Omega}\frac{\partial U}{\partial E_\alpha}, \qquad F_{i,\beta} = -\frac{\partial U}{\partial u_{i,\beta}}. \tag{2.11}$$

In the presence of a homogeneous electric field, the system gains an additional energy term through a coupling to the macroscopic polarization [13]

$$U^{\text{field}} = -\Omega \mathbf{P} \cdot \mathbf{E}. \tag{2.12}$$

This leads to a force contribution on the ions of the form

$$F_{i,\beta}^{\text{field}} = Z_{i,\alpha\beta}^{*} E_{\alpha}. \tag{2.13}$$

For a time-dependent electric field oscillating with frequency ω, the response of a material becomes dynamical rather than purely electrostatic. Lattice vibrations can couple resonantly to an external electric field at specific frequencies, which is described by the dielectric response function $\varepsilon(\omega, \boldsymbol{q})$. It can be decomposed into a real and an imaginary part

$$\varepsilon(\omega, \boldsymbol{q}) = \varepsilon_1(\omega, \boldsymbol{q}) + i\varepsilon_2(\omega, \boldsymbol{q}). \tag{2.14}$$

Both ions and electrons contribute to the dielectric response on different timescales. At high frequencies, only the electronic degrees of freedom can follow the oscillating field, leading to the high-frequency dielectric constant ε_∞. At lower frequencies, ionic motion associated with lattice vibrations also contributes to the polarization.

In the long-wavelength limit ($\boldsymbol{q} \to 0$), the dielectric function takes the form [14]

$$\varepsilon_1(\omega) = \varepsilon_\infty + \frac{4\pi}{3\Omega} \sum_n \frac{\left|\sum_{i,\beta} Z_{i,\alpha\beta}^{*}\, u_{i,\beta}^{n}\right|^2}{\omega^2 - \omega_n^2}, \tag{2.15}$$

$$\varepsilon_2(\omega) = \frac{4\pi^2}{3\Omega} \sum_n \frac{\left|\sum_{i,\beta} Z_{i,\alpha\beta}^{*}\, u_{i,\beta}^{n}\right|^2}{2\omega_n} \delta(\omega - \omega_n), \tag{2.16}$$

where ω_n denotes the phonon frequencies. The long-wavelength limit corresponds to a spatially uniform electric field. In this limit, only phonons near the Γ-point ($\mathbf{q} = 0$) contribute to the dielectric response, since they correspond to collective motions in which all unit cells oscillate in phase. Among these, only optical phonons whose displacements generate a nonzero macroscopic polarization can couple to the electric field. Such modes are called infrared (IR)-active, and correspond to a nonzero numerator $\sum_{i,\beta} Z_{i,\alpha\beta}^{*} u_{i,\beta}^{n} \neq 0$ in the dielectric function.

In practice, the IR spectrum can be obtained from MD simulations as the Fourier transform of the polarization-current autocorrelation function [15]

$$I(\omega) \propto \int_0^\infty \langle \dot{\mathbf{P}}(0) \cdot \dot{\mathbf{P}}(t) \rangle \, e^{-i\omega t}\, dt, \tag{2.17}$$

which is equivalent to the power spectral density (PSD) of $\dot{\mathbf{P}}$ by the Wiener-Khinchin theorem. The time derivative of the macroscopic polarization is given by

$$\dot{P}_\alpha(t) = \frac{1}{\Omega} \sum_i Z_{i,\alpha\beta}^{*} v_{i,\beta}(t), \tag{2.18}$$

with $\mathbf{v}_i(t)$ being the velocity of atom i. Peaks in $I(\omega)$ correspond to IR-active modes that can resonantly couple to an oscillating electric field.

2.3 Thermodynamics of phase transitions

Phase transitions can be described thermodynamically in terms of a suitable free energy functional. In equilibrium, the stable phase corresponds to the state that

minimizes this thermodynamic potential with respect to the relevant degrees of freedom. Phase transitions are characterized by discontinuities in the derivatives of the free energy with respect to natural variables of the system. A first-order transition has a discontinuity in the first derivative, while a second-order transition has a continuous first derivative but a discontinuous second derivative [16].

A quantity used to distinguish between different phases is the order parameter. Order parameters are often associated with a symmetry that is spontaneously broken at a phase transition, taking a value of zero in the high-symmetry phase and a non-zero value in the broken-symmetry phase.

Within Landau theory, the free energy is expressed as an expansion of the order parameter. Assuming that the free energy is analytic in the order parameter η and respects the symmetry of the system, it can be expanded as

$$F(T,\eta) - F_0 = a\eta^2 + \frac{b}{2}\eta^4 + \mathcal{O}(\eta^6). \tag{2.19}$$

To satisfy thermodynamic stability, the coefficient a changes sign at the critical temperature T_c, such that $a = a_0(T - T_c)$, while $b > 0$ is taken as constant. For $T > T_c$, the free energy has a single minimum at $\eta = 0$, whereas for $T < T_c$ it develops two degenerate minima at $\eta = \pm\eta_0$, corresponding to spontaneous symmetry breaking at the phase transition.

An external electric field can be phenomenologically included by adding a linear coupling $-E\eta$ to Eq. (2.19). Above T_c, the field shifts the single minimum to a finite order parameter and below T_c it lifts the degeneracy between the two minima, as illustrated in Figure 2.1.

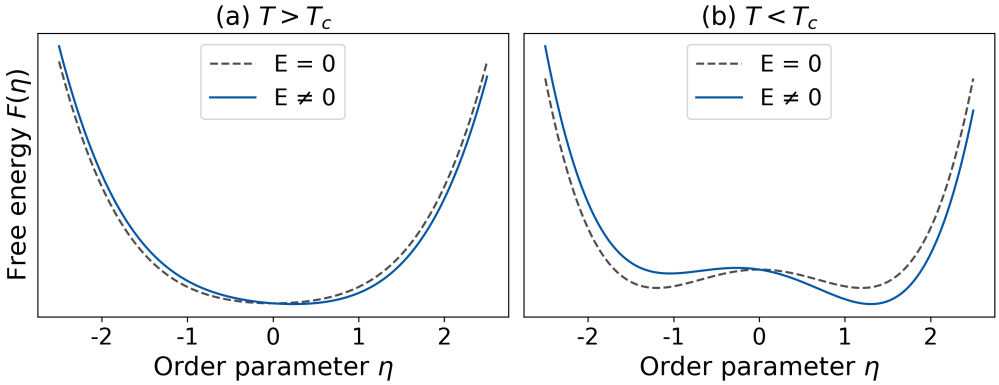

Figure 2.1: Schematic of the Landau free energy above (a) and below (b) the critical temperature T_c. An external electric field favors one of the degenerate minima in the symmetry-broken phase.

Landau theory was originally formulated for second-order phase transitions, but can be extended to describe first-order transitions by including higher-order terms in the free energy expansion. In such cases, metastable states may coexist with the thermodynamically stable phase, which is the microscopic origin of hysteresis. An external field can further break the degeneracy between competing minima, potentially driving field-induced switching between structural states.

2.4 Perovskites

A perovskite is a crystal structure with the generic formula ABX_3, where A and B are cations and X is an anion, forming a framework of corner-sharing BX_6 octahedra. In halide perovskites, the X site is a halogen anion and the B cations are divalent, like Pb^{2+} or Sn^{2+}. The A site can be an inorganic monovalent cation like Cs, or an organic molecular cation like methylammonium (MA), in which case the perovskite is called hybrid [17]. Combining these characteristics gives hybrid halide perovskites, such as methylammonium lead iodide $MAPbI_3$. The molecular cation MA, with full chemical formula $CH_3NH_3^+$, can rotate and carries an electric dipole, introducing additional degrees of freedom compared to fully inorganic halide perovskites such as $CsPbBr_3$. Figure 2.2 visualizes the structure of the prototypical hybrid halide perovskite $MAPbI_3$.

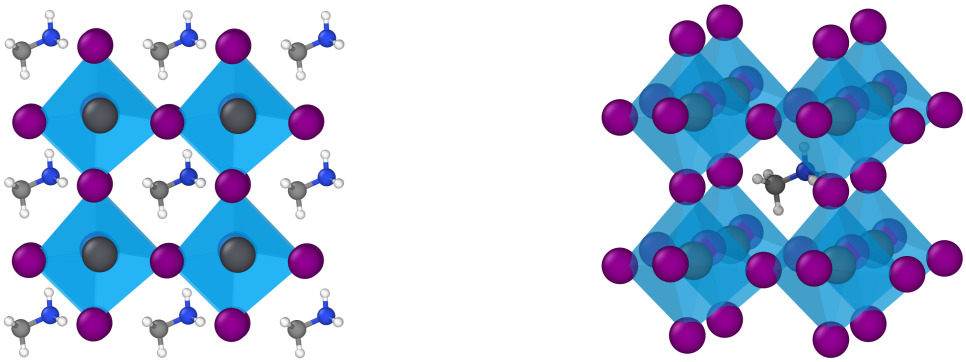

Figure 2.2: Crystal structure of $MAPbI_3$, where the A site is occupied by the MA cation ($CH_3NH_3^+$) and the PbI_6 octahedra form the framework. Atom colors are C (light gray), N (blue), H (white), Pb (gray), and I (purple).

2.4.1 Octahedral tilting

Perovskites often exhibit distortions from the high-symmetry cubic phase at different temperatures, associated with soft phonon modes corresponding to tilting of the BX_6 octahedra. These octahedral tilts can be understood as a structural instability of the cubic phase, resulting in tilted phases with lower symmetry. The octahedra can tilt about any of the three Cartesian directions of the crystal, and successive layers can tilt either in-phase or out-of-phase [18], as illustrated in Figure 2.3.

A common way of describing perovskite structures is through Glazer notation [19], e.g. $a^0b^+c^-$, where a, b and c are the crystallographic directions and the superscripts indicate zero tilt, in-phase or out-of-phase tilt. At room temperature, $MAPbI_3$ adopts the cubic phase, $a^0a^0a^0$, which is untilted. As temperature decreases, $MAPbI_3$ undergoes a transition to the tetragonal $a^0a^0c^-$ phase, characterized by out-of-phase tilting around the c-axis. At lower temperatures, the orthorhombic $a^-a^-c^+$ phase is formed, with both in-phase and out-of-phase tilting [3]. These phases can also be described by their corresponding space groups, with

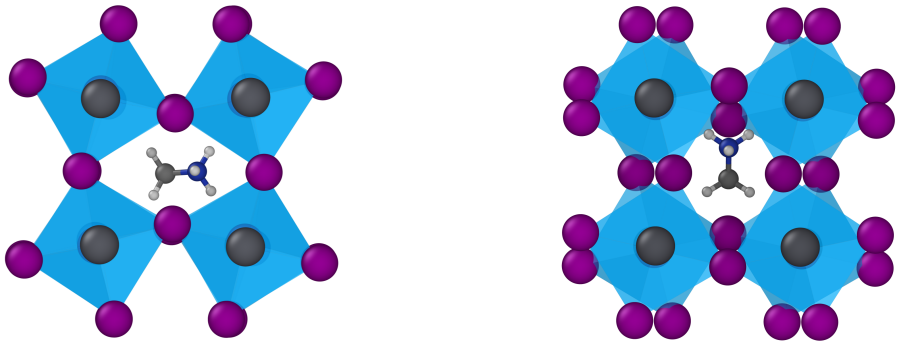

Figure 2.3: Illustration of in-phase (left) and out-of-phase (right) octahedral tilting. The tilt pattern distorts the A-site cavity, constraining the preferred orientation of the MA cation.

the cubic phase belonging to $Pm\bar{3}m$, the tetragonal phase to $I4/mcm$ and the orthorhombic phase to $Pnma$. Some common structural phases of $MAPbI_3$ are summarized in Table 2.1, along with the irreducible representations of the phonon instabilities [20].

Table 2.1: Common structural phases of $MAPbI_3$ described in terms of Glazer tilt systems. Here, R and M denote irreducible representations associated with phonon instabilities at the corresponding Brillouin zone boundary points [20].

Phase	Space group	Glazer notation	Mode(s)
Cubic	$Pm\bar{3}m$	$a^0a^0a^0$	–
Tetragonal	$I4/mcm$	$a^0a^0c^-$	R_4^+
Tetragonal	$P4/mbm$	$a^0a^0c^+$	M_3^+
Orthorhombic	$Pnma$	$a^-a^-c^+$	$R_4^+ + M_3^+$

An ideal cubic perovskite has a lattice parameter of $a = \sqrt{2}(r_A + r_X) = 2(r_B + r_X)$, where r are the ionic radii in ABX_3. Distortions from this structure can be quantified using the Goldschmidt tolerance factor

$$t = \frac{r_A + r_X}{\sqrt{2}(r_B + r_X)}, \tag{2.20}$$

where t is between 0.9 and 1 for a cubic structure. Deviations from $t \approx 1$ indicate that the relative sizes of the ions are not ideally matched, leading to structural distortions. Tilted perovskite structures typically correspond to tolerance factors between 0.71 and 0.9, whereas tolerance factors above 1 or below 0.71 are non-perovskite structures [21].

This geometric mismatch manifests itself in the lattice dynamics as soft phonon modes, corresponding to displacement patterns associated with structural instability. These modes correspond to rotations of the BX_6 octahedra that lower the potential energy of the system. In-phase tilting is associated with M-point modes, whereas out-of-phase tilting corresponds to R-point modes at the Brillouin zone boundary. These zone-boundary modes are highly anharmonic, resulting in a complex potential energy landscape with shallow minima. Although the harmonic approximation

described in Section 2.1 identifies the instabilities via imaginary phonon frequencies, it does not adequately describe the potential energy surface governing the octahedral tilting dynamics. In $MAPbI_3$, the MA molecules play an important role in this complex behavior, as discussed in the next section [6, 7].

2.4.2 The role of methylammonium

The MA cation in $MAPbI_3$ introduces additional degrees of freedom compared to a simple inorganic cation, owing to its ability to rotate and its permanent electric dipole moment. At low temperatures, dipole-dipole interactions favor long-range orientational ordering, while at higher temperatures thermal fluctuations allow increasingly free rotation. The rotational behavior of MA is strongly coupled to the surrounding PbI_6 octahedral framework. As the symmetry of the inorganic cage is lowered by octahedral tilting, the available orientational space for MA narrows. Two main effects are believed to contribute to this cage-molecule coupling. Hydrogen bonding between the ammonium group of MA and the iodide anions creates preferred orientations relative to the cage geometry. Steric interactions additionally restrict configurations in which atoms are brought too close together [22]. While these interactions are not directly investigated in this work, they provide the microscopic basis for the coupling between MA orientations and the inorganic framework.

3
Methods

This section describes the computational methods employed to investigate electric field-induced phase transitions in $MAPbI_3$. The first part covers the theoretical foundations of MD simulations and the charge-aware neuroevolution potential, which is trained on density functional theory calculations. The second part details the specific implementation and post-processing methods for extracting structural order parameters and phase behavior.

3.1 Molecular dynamics

MD is a well-established computational method for simulating the time evolution of many-particle systems [23]. In MD, Newton's equations of motion are solved numerically using interatomic forces to propagate the positions, velocities and accelerations of all particles in time. The force acting on each particle, i, is obtained as the gradient of the total potential energy U,

$$\boldsymbol{F}_i = -\frac{\partial U}{\partial \boldsymbol{r}_i}. \tag{3.1}$$

In this work, U is provided by a neuroevolution potential (NEP) trained to reproduce the potential energy surface of the perovskite system. To propagate the system in time, the equations of motion are discretized using a Taylor expansion of the atomic positions around time t. Adding the forward $(t+\Delta t)$ and backward $(t-\Delta t)$ expansions eliminates all odd-order contributions, resulting in the Verlet algorithm

$$\boldsymbol{r}_i(t+\Delta t) = 2\boldsymbol{r}_i(t) - \boldsymbol{r}_i(t-\Delta t) + \boldsymbol{a}_i(t)\Delta t^2 + \mathcal{O}(\Delta t^4), \tag{3.2}$$

where the acceleration is given by $\boldsymbol{a}_i(t) = \boldsymbol{F}_i(t)/m_i$. Velocities can be obtained by instead subtracting the Taylor expansions at $t+\Delta t$ and $t-\Delta t$, giving

$$\boldsymbol{v}_i(t) = \frac{1}{2\Delta t}\left[\boldsymbol{r}_i(t+\Delta t) - \boldsymbol{r}_i(t-\Delta t)\right] + \mathcal{O}(\Delta t^2). \tag{3.3}$$

To avoid the need for previous-step positions, the algorithm is reformulated into the velocity Verlet form, where positions and velocities are updated simultaneously

$$\begin{aligned} \boldsymbol{r}_i(t+\Delta t) &= \boldsymbol{r}_i(t) + \boldsymbol{v}_i(t)\Delta t + \frac{1}{2}\boldsymbol{a}_i(t)\Delta t^2 \\ \boldsymbol{v}_i(t+\Delta t) &= \boldsymbol{v}_i(t) + \frac{1}{2}\left[\boldsymbol{a}_i(t) + \boldsymbol{a}_i(t+\Delta t)\right]\Delta t. \end{aligned} \tag{3.4}$$

These equations constitute the basis for MD simulations implemented in the `GPUMD` package used in this work.

3.2 Sampling thermodynamic ensembles

The data resulting from MD simulations are particle trajectories. From these trajectories, ensemble-averaged quantities can be computed that correspond to experimentally measurable observables. In the MD method discussed in the previous section, the system is sampled in the microcanonical (NVE) ensemble, i.e., with a constant number of particles, volume, and energy. Other ensembles are often more convenient depending on the control variables of interest.

3.2.1 The canonical ensemble

A system in thermal equilibrium with a heat bath is described by the canonical (NVT) ensemble, where the temperature is fixed instead of the total energy. To control the temperature in MD simulations, the Berendsen thermostat [24] can be used to rescale velocities as

$$\boldsymbol{v}_i \to \lambda \boldsymbol{v}_i \quad \text{with} \quad \lambda = \sqrt{1 + \frac{\Delta t}{\tau_T}\left(\frac{T_0}{T} - 1\right)} \tag{3.5}$$

where Δt is the timestep in MD, τ_T is the time constant of the coupling, T_0 is the target temperature and T is the current temperature.

The Berendsen thermostat is mostly used for reaching equilibrium. For sampling the canonical ensemble, the Nosé-Hoover chain thermostat [25] is more suitable. In this method, the equations of motion are modified by an additional friction term acting on the particle velocities,

$$\frac{d\boldsymbol{v}_i}{dt} = \boldsymbol{a}_i - \frac{\pi_0}{Q_0}\boldsymbol{v}_i \tag{3.6}$$

where Q_0 is the mass associated with the thermostat variable and π_0 its conjugate momentum.

3.2.2 The isobaric-isothermal ensemble

A system that is coupled to a bath with fixed temperature and pressure corresponds to the isothermal-isobaric (NPT) ensemble. To control the temperature in MD simulations, the Berendsen thermostat is used as in Eq. (3.5). The pressure is controlled with the Berendsen barostat [24] that rescales the simulation box, $\boldsymbol{h}$, and positions with a 3×3 scaling matrix, $\boldsymbol{\mu}$,

$$\boldsymbol{r}_i \to \boldsymbol{\mu}\boldsymbol{r}_i, \quad \boldsymbol{h} \to \boldsymbol{\mu}\boldsymbol{h}. \tag{3.7}$$

For a triclinic simulation box, the components of the scaling matrix are

$$\mu_{\alpha\beta} = 1 - \frac{\beta_{\alpha\beta}\Delta t}{3\tau_p}\left(p_{\alpha\beta}^{\text{target}} - p_{\alpha\beta}^{\text{instant}}\right) \tag{3.8}$$

where $\beta_{\alpha\beta}$ is the isothermal compressibility, Δt is the timestep and τ_p is the time constant of the pressure coupling. A limitation of the Berendsen thermo- and barostats is that they do not generate correct volume fluctuations. To address this, the Berendsen method is extended by including a stochastic cell rescaling (SCR) barostat [26].

3.3 Density functional theory

Density functional theory (DFT) is an *ab initio* (from first principles) computational method used to determine the electronic structure of many-body systems [27], and forms the basis of the training data for the machine-learned potential used in this work.

In the context of lattice dynamics, interatomic forces are governed by the redistribution of the electron density as the nuclei move. Determining these forces theoretically requires solving for the total energy E in the time-independent many-body Schrödinger equation,

$$\hat{H}\Psi = E\Psi, \tag{3.9}$$

where the electronic state is described by the wavefunction $\Psi(\boldsymbol{r}_1, \boldsymbol{r}_2, \ldots, \boldsymbol{r}_N)$. The Hamiltonian $\hat{H}$ for a system of N electrons moving in the field of fixed nuclei (within the Born-Oppenheimer approximation) is given by

$$\hat{H} = \hat{T} + \hat{V} + \hat{U} = \sum_{i=1}^{N} \left(-\frac{\hbar^2}{2m_i} \nabla_i^2 \right) + \sum_{i=1}^{N} V(\boldsymbol{r}_i) + \frac{1}{2} \sum_{i \neq j}^{N} \frac{1}{|r_i - r_j|}, \tag{3.10}$$

where $\hat{T}$ is the kinetic energy, $\hat{V}$ is the external potential from the nuclei and $\hat{U}$ is the electron-electron interaction. The ground-state energy and wavefunction are obtained variationally by minimizing the energy functional $E[\Psi]$.

DFT reformulates this complex many-body problem in terms of the electron density $n(\mathbf{r})$. According to the Hohenberg-Kohn theorems [28], the external potential $V(\boldsymbol{r})$ is uniquely determined, up to a constant, by $n(\mathbf{r})$. Since $V(\boldsymbol{r})$ determines all properties of the system, the ground-state is a unique functional of the electron density, which can then be written as $E[n]$. Furthermore, the exact ground-state density minimizes $E[n]$.

Kohn-Sham theory provides a practical framework to find this density [29]. The interacting system is mapped onto an auxiliary system of non-interacting electrons moving in an effective potential $V_{\text{eff}}(\boldsymbol{r})$ that reproduces the same ground-state density. The resulting Kohn-Sham equations

$$\left(-\frac{\hbar^2}{2m} \nabla^2 + V_{\text{eff}}(\boldsymbol{r}) \right) \varphi_i(\boldsymbol{r}) = \varepsilon_i \varphi_i(\boldsymbol{r}) \tag{3.11}$$

are eigenvalue equations for the Kohn-Sham single-particle orbitals $\varphi_i(\boldsymbol{r})$ with eigenvalues ε_i. The solution yields the density as $n(\boldsymbol{r}) = \sum_{i=1}^{N} |\varphi_i(\boldsymbol{r})|^2$, from which the total energy functional and interatomic forces can be obtained.

3.4 Neuroevolution potential

The NEP is a type of machine-learned potential that provides the potential energy U and forces in an MD simulation, as in Eq. (3.1). DFT calculations are used as training data. The free parameters in the NEP have been optimized via the separable natural evolution strategy [30, 31]. In the `GPUMD` implementation [10], the

site energy of atom i is modeled using a feedforward neural network with one hidden layer

$$U_i = \sum_{\mu=1}^{N_{\rm neu}} w_\mu^{(1)} \tanh\left(\sum_{\nu=1}^{N_{\rm des}} w_{\mu\nu}^{(0)} D_\nu^i - b_\mu^{(0)}\right) - b^{(1)}, \tag{3.12}$$

where $\boldsymbol{w}^{(0)}$ and $\boldsymbol{w}^{(1)}$ are weights, $\boldsymbol{b}^{(0)}$ and $\boldsymbol{b}^{(1)}$ are biases, and $\tanh(x)$ is the activation function in the hidden layer. Furthermore, $N_{\rm neu}$ is the number of neurons and $N_{\rm des}$ is the number of descriptors, resulting in a total number of parameters $(N_{\rm des}+2)N_{\rm neu}+1$. The descriptors, D_ν^i, are mathematical representations of the atomic environment, and consist of radial and angular parts. The radial descriptor consists of a summation of functions over all neighbors of atom i, up to a certain cutoff radius. Finally, the total potential energy is obtained as the sum over all atom contributions,

$$U^{\rm NEP} = \sum_i U_i. \tag{3.13}$$

3.5 Charge-aware neuroevolution potential

The finite cutoff radius in the descriptor construction makes conventional NEP models inherently short-ranged. For simulations involving an applied external electric field, the model needs to include long-range electrostatic interactions and a way to couple to the field. To this end, this work uses the recently developed charge-aware neuroevolution potential (qNEP) architecture [32].

The qNEP extends the NEP architecture by adding the partial charge q_i as a second output node, in addition to the site energy U_i in Eq. (3.12). The partial charges are environment-dependent, allowing the model to capture polarization effects and other electrostatic phenomena. Charge conservation is enforced during training through an additional constraint on the total charge.

From the predicted partial charges, the electrostatic energy $U^{\rm ES}$ is evaluated using Ewald decomposition including both real-space and reciprocal-space components (mode 1). The total energy is given by the sum of the conventional NEP energy and the electrostatic energy,

$$U^{\rm tot} = U^{\rm NEP} + U^{\rm ES}. \tag{3.14}$$

Furthermore, the macroscopic polarization is evaluated as

$$P_\alpha = \sum_i \sqrt{\varepsilon_\infty}\, q_i, \tag{3.15}$$

from which the Born effective charges (BEC) are obtained (see Section 2.2). The total force acting on each atom is given by the sum of the short-ranged NEP force, the electrostatic force arising from $U^{\rm ES}$ and the field-induced contribution,

$$\boldsymbol{F}_i = -\nabla_i U^{\rm tot} + \boldsymbol{F}_i^{\rm field}. \tag{3.16}$$

where the field-induced force is obtained from the BEC according to Equation (2.13). Without any applied electric field, $\boldsymbol{F}_i^{\rm field} = 0$.

3.6 Computational details

All simulations were performed on a system of 32 928 atoms (a $14\times14\times14$ repetition of the primitive cell), unless explicitly stated otherwise. Heating and cooling runs were performed between 1 K and 450 K in the isobaric-isothermal (NPT) ensemble, with a heating and cooling rate of 11.25 K/ns. The supercell size was chosen to minimize finite-size effects and the rate was chosen to ensure quasi-static conditions at each temperature. MD simulations were run on graphical processing units using the `GPUMD` package [10] with a timestep of 0.5 fs, chosen to resolve the motion of the light hydrogen atoms. Interatomic forces were evaluated in the MD simulations using a charge-aware qNEP model constructed outside the scope of this thesis [32]. Several software packages were used for post-processing: `ASE` [33], `Calorine` [34], `dynasor` [35, 36], `hiphive` [37] and `OVITO` [38]. Specific computational details are explained in the following subsections.

3.6.1 Structural order parameters

Octahedral tilt angles, obtained from the local rotation of each PbI_6 octahedron relative to the ideal cubic reference structure, were used as structural order parameters to identify phase transitions. For each PbI_6 octahedron, the six Pb–I bonds were identified and matched to the corresponding ideal cubic perovskite environment following the procedure in [39], implemented in `OVITO`. From this mapping, the resulting rotation was converted to Euler angles $\theta_x, \theta_y, \theta_z$ with the `SCIPY` package [40]. Among the possible Euler angle conventions, the one yielding angles in increasing magnitude was selected, consistent with the Glazer convention. Tilt angle distributions were extracted for each trajectory snapshot, providing a continuous representation as a function of temperature.

A complementary order parameter is the phonon mode projection [41], which quantifies the amplitude of atomic displacements $\boldsymbol{u}(t)$ along a mode eigenvector $\boldsymbol{e}_\lambda$,

$$Q_\lambda(t) = \boldsymbol{u}(t) \cdot \boldsymbol{e}_\lambda. \tag{3.17}$$

Atomic displacements were computed relative to the ideal cubic reference structure using `hiphive` [37]. M- and R-point eigenvectors were obtained with `PHONOPY` [42] and the mode projection amplitudes Q_M and Q_R were computed with `dynasor` [35, 36].

A third measure of lattice distortion is B-site off-centering (here B=Pb), defined as

$$\boldsymbol{d}_i = \boldsymbol{r}_{\mathrm{Pb},i} - \frac{1}{6}\sum_{j\in\mathcal{N}(i)} \boldsymbol{r}_{\mathrm{I},j}, \tag{3.18}$$

where i indexes the PbI_6 octahedra and $j \in \mathcal{N}(i)$ labels the six I atoms belonging to octahedron i. The quantity $\boldsymbol{d}_i$ measures the displacement of the Pb atom relative to the octahedral centroid, in all three Cartesian directions $\boldsymbol{d}_i = (d_{i,x}, d_{i,y}, d_{i,z})$. To probe field-induced polar distortions, the Pb off-centering vectors were averaged over all octahedra,

$$\langle \boldsymbol{d} \rangle = \frac{1}{N_{\mathrm{Pb}}} \sum_{i=1}^{N_{\mathrm{Pb}}} \boldsymbol{d}_i, \tag{3.19}$$

for each snapshot of the heating trajectories.

3.6.2 Characterization of MA cation orientations

MA cation orientations were quantified using spherical coordinates of the C–N bond vector $\boldsymbol{r}_{\mathrm{CN}}$, as illustrated in Figure 3.1. In a crystal-aligned coordinate system, the polar and azimuthal angles were defined as

$$\theta = \arccos \hat{r}^z_{\mathrm{CN}}, \qquad \phi = \arctan 2(\hat{r}^y_{\mathrm{CN}}, \hat{r}^x_{\mathrm{CN}}), \tag{3.20}$$

where $\hat{\boldsymbol{r}}_{\mathrm{CN}}$ is the normalized bond vector.

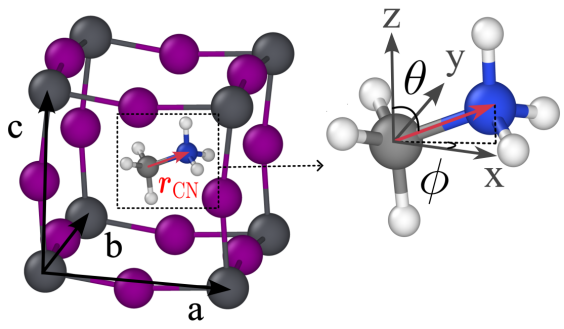

Figure 3.1: MA cation inside the Pb−I octahedral cage. The C-N bond vector (red arrow) defines the MA orientation via polar angle θ and azimuthal angle ϕ in a Cartesian coordinate system aligned with the crystal axes (a, b, c).

A consistent classification of orientations requires distinguishing between the simulation (lab) frame and the intrinsic crystal coordinate system. In MD simulations, symmetry-equivalent choices of the unit cell may lead to arbitrary orientations of the octahedral tilt axes with respect to the Cartesian directions. To remove this ambiguity, the simulation frame was rotated such that the main tilt axis aligns with the crystallographic z-direction, following the Glazer notation. Throughout this work, crystallographic directions are denoted a, b, c and simulation frame directions as X, Y, Z. This approach is commonly used in perovskite MD studies in the absence of external fields.

In the presence of an external electric field, the symmetry between parallel and antiparallel orientations is explicitly broken, introducing a directional bias. Nevertheless, to isolate the coupling between the MA cations and the inorganic framework from field-induced frame reorientation, the coordinate system was defined using the same crystal-alignment procedure as in the zero-field case.

Within this crystal frame, crystallographic reference directions $\langle 100 \rangle$, $\langle 110 \rangle$, and $\langle 111 \rangle$ were defined. In tetragonal and orthorhombic phases, the symmetry-equivalence of these directions is broken, unlike in the ideal cubic perovskite. Yet they remain useful descriptors due to the pseudo-cubic nature of $MAPbI_3$, with lattice parameters that are nearly equal and interaxial angles close to 90°.

To characterize rotational dynamics of MA, the orientational autocorrelation function (ACF) was computed as

$$C(\tau) = \frac{\langle \boldsymbol{r}_{\mathrm{CN},i}(t) \cdot \boldsymbol{r}_{\mathrm{CN},i}(t+\tau) \rangle}{\langle \boldsymbol{r}_{\mathrm{CN},i}(t) \cdot \boldsymbol{r}_{\mathrm{CN},i}(t) \rangle}, \tag{3.21}$$

where i denotes the i-th MA molecule and the average is taken over all molecules. The ACF quantifies the memory of previous molecular orientations, decaying from unity at $\tau = 0$ to zero as orientational memory is lost.

3.6.3 Phase diagram construction

For the field-temperature (E-T) phase diagrams, phase boundaries were extracted from heating and cooling simulations under different electric field strengths using phonon mode projections and octahedral tilt angles as order parameters. The electric field was applied in the simulation Z-direction, corresponding to a face of the pseudocubic structure. Transition temperatures were extracted for 15 field strengths, with $0.005\,\mathrm{V/Å}$ spacing in the first half of the interval and $0.01\,\mathrm{V/Å}$ spacing in the second half. The maximum field strength was chosen to remain below the field emission threshold of $MAPbI_3$. Field emission in $MAPbI_3$ nanorods has been reported at local fields of approximately $1.87\,\mathrm{V/Å}$ [43], providing a conservative upper bound for bulk where no geometric enhancement is present.

The frequency-temperature (f-T) phase diagrams were constructed in a similar way, applying an oscillating field $E(t) = E_0 \sin(2\pi f t)$ for a fixed field strength E_0 and different frequencies f. Based on the E-T phase diagram, one low field $0.01\,\mathrm{V/Å}$ and one intermediate field $0.03\,\mathrm{V/Å}$ were chosen. Frequencies were chosen in the range of $0.001\,\mathrm{THz}$ to $20\,\mathrm{THz}$, with 24 points distributed on a logarithmic grid and denser sampling near resonant behavior. This range was selected to span the relevant dynamical timescales of the system, from slow structural dynamics of the PbI_6 framework to faster intramolecular vibrational modes of the MA cation.

4

Results

This chapter presents the results of molecular dynamics simulations investigating electric field-induced phase transitions in $MAPbI_3$. The first part validates the qNEP model used throughout the study. The second part characterizes the phase behavior and MA cation dynamics at zero field, establishing a baseline for all subsequent analyses. The third and fourth parts examine the structural response to static and oscillating electric fields, respectively, revealing field-induced shifts in phase transition temperatures and resonant coupling to framework vibrational modes.

4.1 NEP model

The NEP model used in this work is a mode-1 qNEP model with 30 neurons in the hidden layer, using radial and angular cutoffs of 8 Å and 4 Å, respectively. Two-stage training was performed using `GPUMD`. The first stage prioritized accurate force predictions with the force loss parameter $\lambda_f = 10$ and energy loss parameter $\lambda_e = 1$. The second stage refined the potential by balancing energy and force predictions equally with $\lambda_f = \lambda_e = 5$. Figure 4.1 shows parity plots comparing predicted quantities to DFT reference calculations during training.

The model achieves high R^2-scores for all target properties, with $R^2 \gtrsim 0.985$. Energies are reproduced with particularly high accuracy, while forces and higher-order quantities show slightly lower but still good agreement. The loss curves and RMSE metrics decrease over the course of training (Figure 4.2), indicating successful model convergence. A clear change in behavior is observed at 2×10^5 generations, corresponding to the transition to the second training stage with modified loss weights.

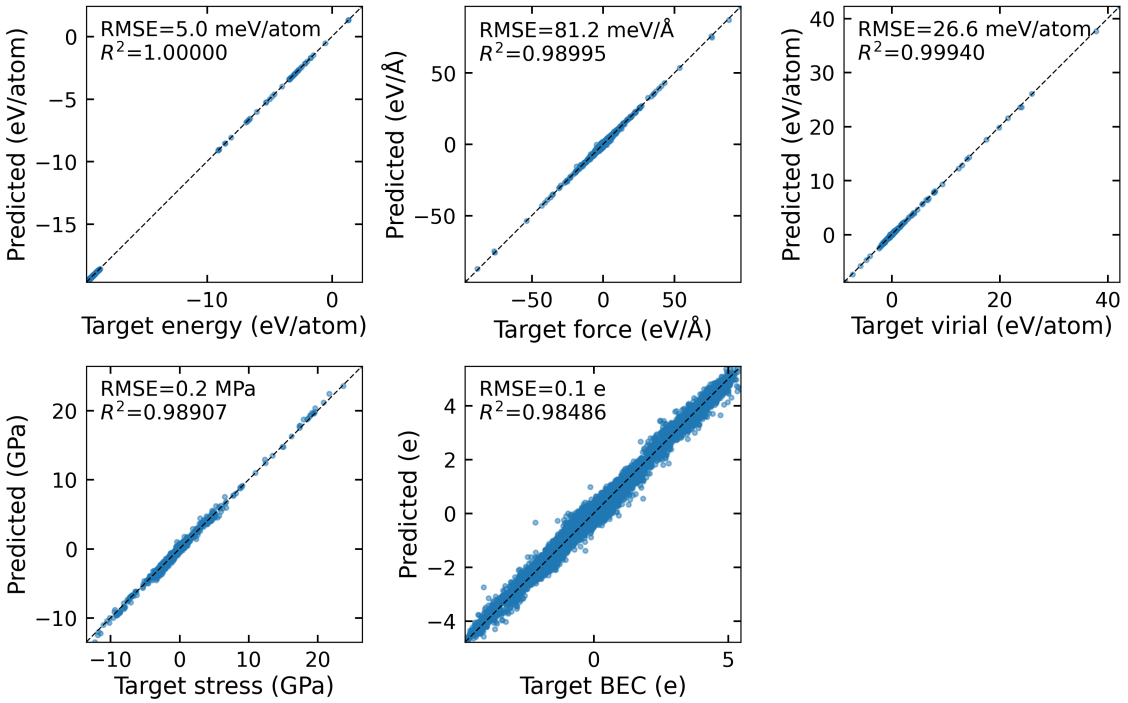

Figure 4.1: Training parity plots comparing predicted energies, forces, virials, stresses and BEC with DFT calculations. The root-mean-square error (RMSE) and R^2-score are indicated for each quantity.

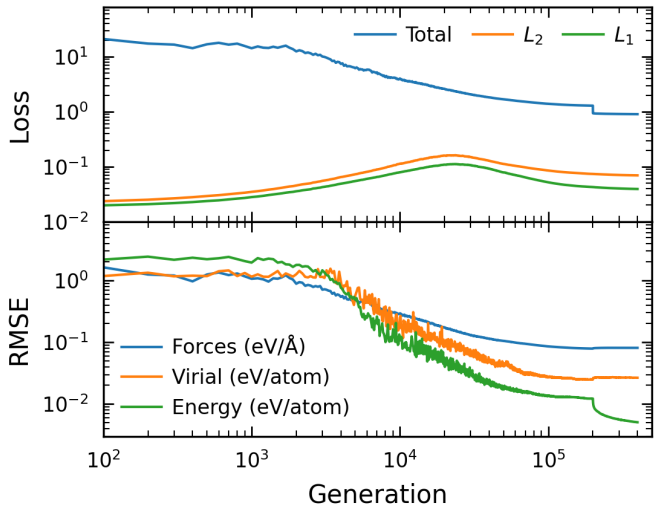

Figure 4.2: Loss function and RMSE during training. The total loss function and regularization terms L_1, L_2 are shown. The step at 2×10^5 generations represents the second stage of training, where the model found a new minimum.

4.2 Phase behavior at zero field

To obtain a baseline for all further investigations, the phase behavior of $MAPbI_3$ was first characterized without any external fields, focusing on phase transitions and

MA cation orientations. Figure 4.3 shows the lattice parameters together with the M- and R-point phonon mode projections during heating and cooling simulations.

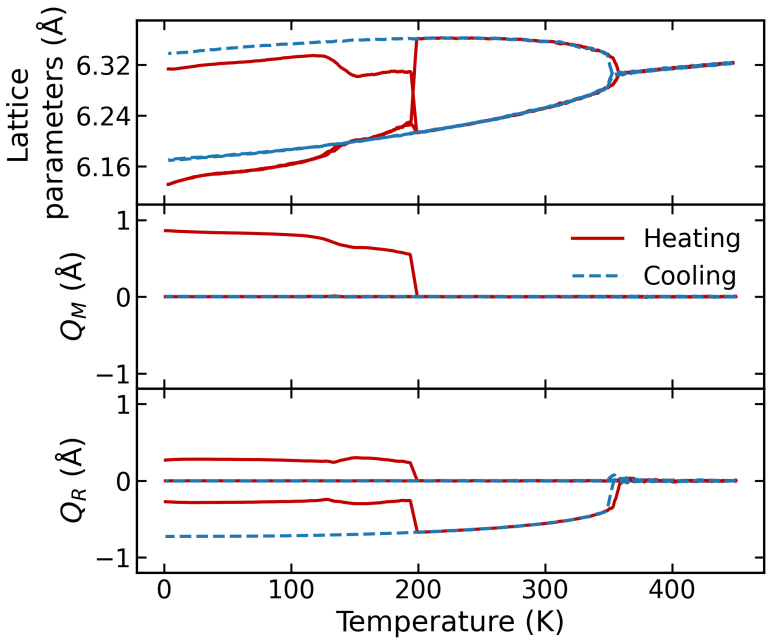

Figure 4.3: Lattice parameters and mode projections from heating (red solid line) and cooling (blue dashed line) of $MAPbI_3$.

Upon heating, $MAPbI_3$ started from the orthorhombic $a^-a^-c^+$ structure with three activated modes: one M-mode (in-phase) and two R-modes (out-of-phase). Note that the different signs of Q_M and Q_R are arbitrary and depend on the eigenvector convention, they do not affect the physical interpretation of in-phase vs out-of-phase tilting. The smooth variation in lattice parameters and mode amplitudes around 130 K does not correspond to a phase transition. It is instead attributed to a transient equilibration effect, likely associated with the system relaxing from the initial configuration towards the thermodynamically stable orthorhombic structure under finite-temperature dynamics.

At 200 K, only the R_z mode remains activated, indicating a transition to the tetragonal $a^0a^0c^-$ structure. At 360 K, all modes average to zero, consistent with the cubic $a^0a^0a^0$ structure. Upon cooling, the system starts from the cubic structure and transitions to the tetragonal $a^0a^0c^-$ structure at 355 K, where it remains at lower temperatures. This lag upon cooling is called hysteresis and has been observed in previous studies of $MAPbI_3$. It indicates that the orthorhombic-to-tetragonal transition is first-order with a large energy barrier, leaving the system trapped in a metastable tetragonal state upon cooling [44, 45]. In experiments, the orthorhombic-to-tetragonal transition has been observed at 160 K and the tetragonal-to-cubic transition at 330 K [46], i.e., approximately 30 K lower than the transition temperatures found in this simulation. Such discrepancies are common when using machine-learned interatomic potentials trained on DFT data.

Figure 4.4 shows the evolution of the lattice angles extracted from the simulation

cell during heating. In ideal crystallography, the lattice angles should be orthogonal, $\alpha = \beta = \gamma = 90°$, for all three phases. A small deviation of the β angle to approximately 88.5° is observed in the orthorhombic phase. This originates from shear fluctuations of the fully flexible (triclinic) NPT simulation cell. Upon heating towards the orthorhombic-to-tetragonal transition, β gradually increases and slightly overshoots above 90° before converging, reflecting relaxation of shear strain under the applied barostat.

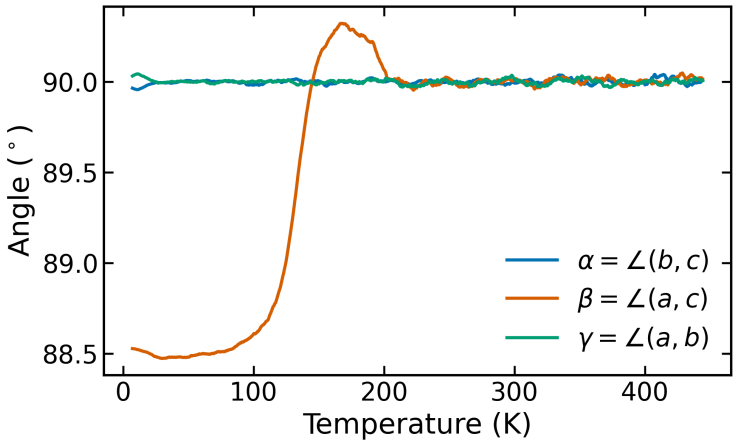

Figure 4.4: Evolution of the unit cell lattice angles α, β and γ during heating. The orthorhombic-to-tetragonal transition is visible as β converges to 90°.

In addition to the mode projection order parameters, octahedral tilt angles were extracted from heating and cooling simulations, shown in Figure 4.5. The same phase transition from orthorhombic to tetragonal is observed for heating at 200 K, and subsequently from tetragonal to cubic at 360 K. As before, the system exhibits hysteresis upon cooling, where only the cubic-to-tetragonal transition at 355 K appears. In the orthorhombic $a^-a^-c^+$ phase, tilting about the c-axis is substantially larger than about the a- and b-axes, making the c-axis the dominant tilting direction in this phase.

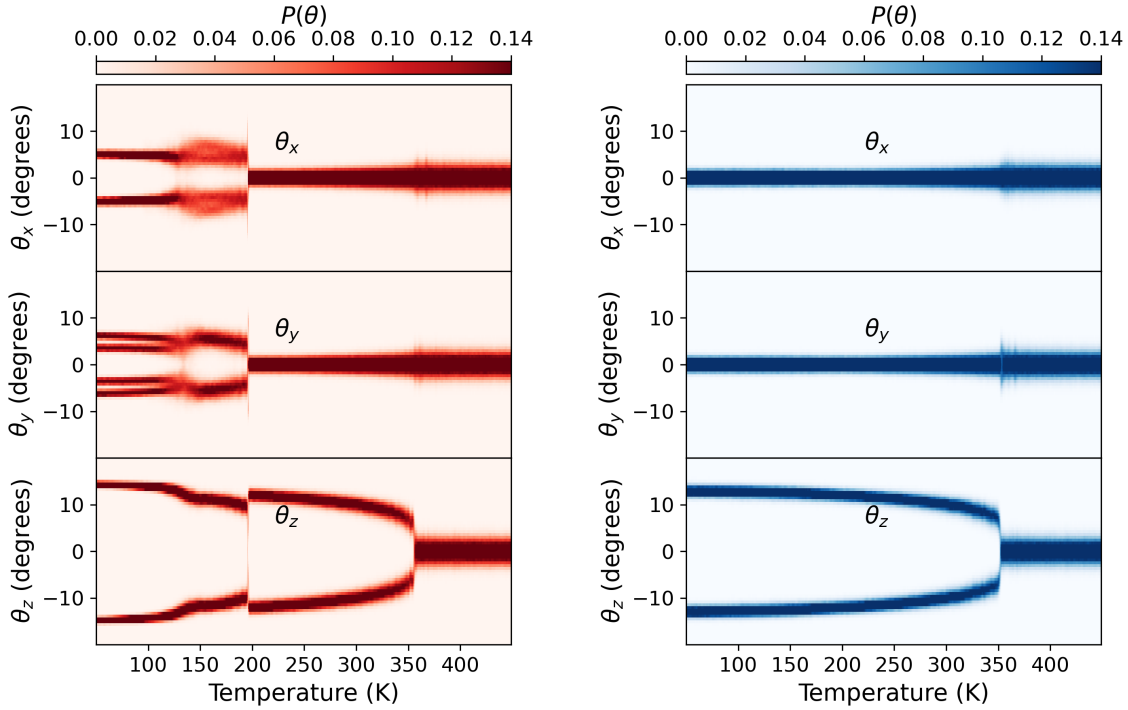

Figure 4.5: Distributions of octahedral tilt angles during heating (left) and cooling (right). During heating, the phase transitions at 200 K and 360 K are visible. During cooling, a clear hysteresis is observed, where the cubic-to-tetragonal transition occurs at 355 K, while the tetragonal-to-orthorhombic transition is suppressed.

From the heating simulations, the orientations of the $\boldsymbol{r}_{\mathrm{CN}}$ vectors were extracted within the crystal frame, according to the method described in Section 3.6.2. Three representative temperatures for the phases of $MAPbI_3$ were chosen: orthorhombic $a^-a^-c^+$ at 150 K, tetragonal $a^0a^0c^-$ at 250 K and cubic $a^0a^0a^0$ at 400 K. The distributions of the spherical angles of $\boldsymbol{r}_{\mathrm{CN}}$, shown in Figure 4.6, were obtained by averaging the trajectory within a window of ± 10 K around each target temperature.

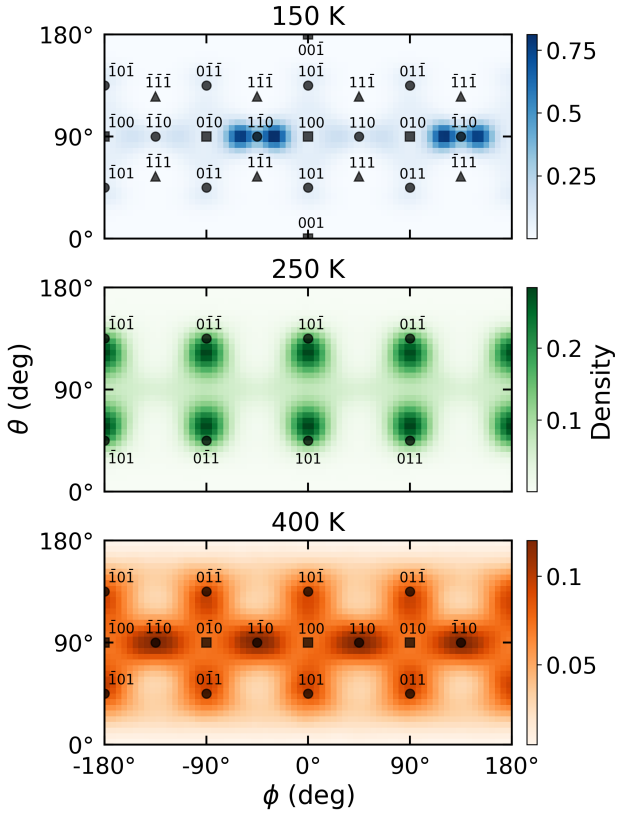

Figure 4.6: Distribution of the C−N bond vector in MA molecules, at three representative temperatures. ϕ is the azimuthal angle, measured in the crystallographic ab plane and θ is the polar angle, measured from the crystallographic c-axis. The markers denote crystallographic direction families $\langle 100 \rangle$ (squares), $\langle 110 \rangle$ (circles) and $\langle 111 \rangle$ (triangles) for reference.

In the low-temperature orthorhombic structure, the MA molecules occupy four distinct orientations. Of the two leftmost spots in the 150 K plot, one spot is located between $[0\bar{1}0]$ and $[1\bar{1}0]$, and the other between $[1\bar{1}0]$ and $[100]$. The two rightmost spots appear at the corresponding 180° rotated positions in the azimuthal angle. Residual density at additional spots reflects traces from the structural relaxation discussed above. Prior to this relaxation, the MA molecules occupied four spots similar to the present ones, but rotated by 90°. The angles extracted from the maxima in density of the four spots are: $\theta = 92°$, $\phi \in \{-58°, -28°, 122°, 152°\}$.

At intermediate temperatures, in the tetragonal structure, the MA molecules are distributed over eight different directions close to the $\langle 110 \rangle$ family. A finite probability density is observed between these points, indicating reorientation between states. Of the 12 different $\langle 110 \rangle$ directions, four are not observed, corresponding to those lying in the ab plane. The corresponding angles are $\theta \in \{58°, 122°\}$, $\phi \in \{-178°, -88°, -2°, 88°\}$.

Finally, in the high-temperature cubic structure, the molecules show increased orientational disorder. They occupy all $\langle 110 \rangle$ directions, with about equal probability. Orientations pointing directly along the $\langle 100 \rangle$ directions are comparatively suppressed. An enhanced density near the equator ($\theta \approx 90°$) partly stems from the

geometric stretching inherent to spherical projection. The angles, in addition to the tetragonal-phase angles, are $\theta = 90°$, $\phi \in \{-132°, -42°, 42°, 132°\}$.

The observed evolution follows the change in octahedral tilt pattern shown in Figure 4.5. In the orthorhombic phase, the full $a^-a^-c^+$ tilt lowers the symmetry of the inorganic cage, restricting MA orientations to a small set of minima within the *ab* plane. In the tetragonal phase, where only *c*-axis tilting remains, the increased symmetry allows occupation of ⟨110⟩-like orientations, with thermally activated transitions between them. This increase in orientational freedom with temperature is consistent with previous MD studies [47]. In the cubic phase, the nearly isotropic cage leads to broad orientational disorder. Ab initio MD studies of the cubic phase report a preference for ⟨110⟩ directions, which has been attributed to favorable hydrogen-bonding with the iodide framework [48].

To complement the static picture of MA orientations, the orientational ACF $C(\tau)$ was computed for several temperatures according to Equation (3.21). Starting from the target temperature in the NPT ensemble, each system was equilibrated for 1 ns in the NVT ensemble. Production runs of 200 ps were subsequently performed in the NVE ensemble, from which MA orientations were sampled. Since rotational timescales in the orthorhombic phase exceed the simulation length, only tetragonal and cubic phase temperatures are included in Figure 4.7.

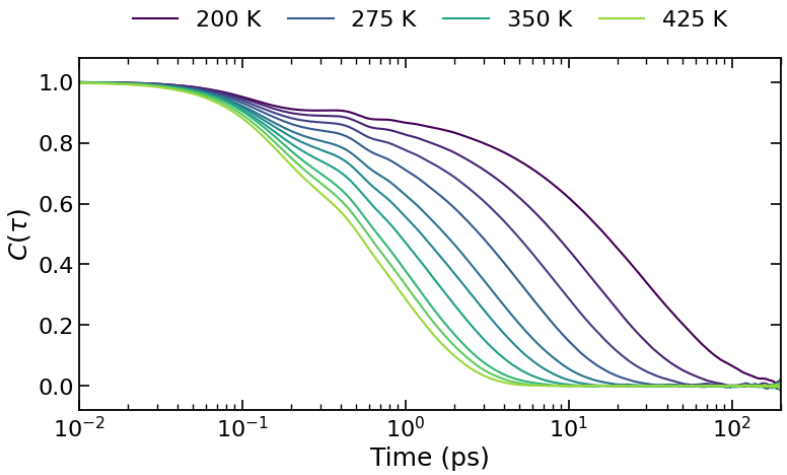

Figure 4.7: Orientational autocorrelation function of MA at temperatures in the tetragonal and cubic phases. The spacing between the lines is 25 K. The decay reflects reorientation between preferred orientations, with a characteristic timescale that decreases strongly with temperature.

At all temperatures, $C(\tau)$ decays from unity, reflecting loss of orientational memory as MA molecules reorient between preferred directions. A characteristic timescale τ_{rot} was extracted by fitting to a single exponential $C(\tau) \propto e^{-\tau/\tau_{\text{rot}}}$, yielding a strong temperature dependence: from $\tau_{\text{rot}} \approx 20$ ps at 200 K to $\tau_{\text{rot}} \approx 2$ ps at 300 K and $\tau_{\text{rot}} \approx 0.9$ ps at 400 K. A slight inflection or shoulder is visible in the early decay, especially at low temperatures, attributed to faster atomic vibrations. The molecular reorientation rate, defined as the inverse rotational timescale, follows an

Arrhenius-type temperature dependence,

$$\frac{1}{\tau_{\mathrm{rot}}(T)} = \frac{1}{\tau_0} e^{-E_A/(k_B T)}, \tag{4.1}$$

where E_A is the activation energy for molecular reorientation, k_B is Boltzmann's constant and τ_0 is the rotation time limit in the absence of energy barrier. Taking the logarithm yields a linear relation between $\ln(1/\tau_{\mathrm{rot}})$ and $1/T$, enabling extraction of E_A from the slope. Figure 4.8 shows the reorientation rate $1/\tau_{\mathrm{rot}}$ as function of temperature together with the Arrhenius fits for the tetragonal and cubic phase.

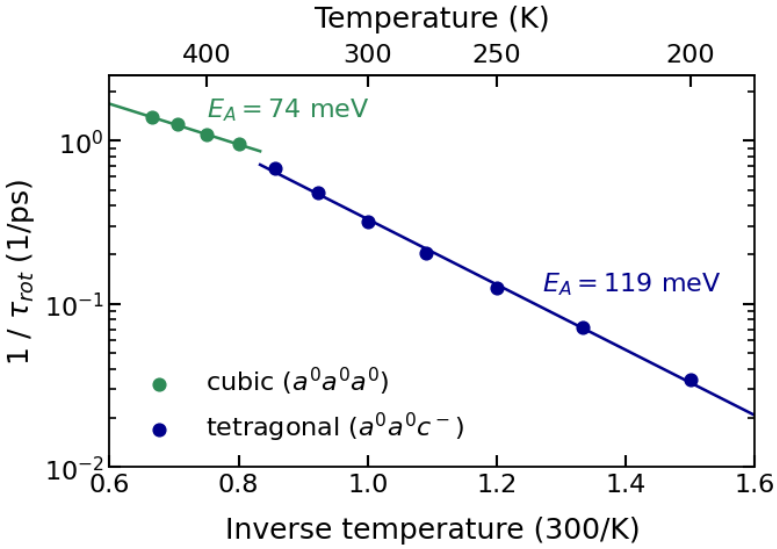

Figure 4.8: Molecular reorientation rate as function of temperature, evaluated at 25 K intervals. Solid lines show Arrhenius fits to each phase separately.

The extracted activation energies are 119 meV for the tetragonal phase and 74 meV for the cubic phase. The tetragonal value agrees well with a previous MD study using a conventional NEP, which reported 120 meV, though the data show some scatter around the fitted line. The cubic value is lower than the previously reported 103 meV [44] but exhibits a better fit to the Arrhenius relation.

To gain insight into the energy landscape of $MAPbI_3$ captured by the qNEP, an energy distribution analysis was performed on 10 000 randomly initialized structures. Each structure was constructed from a $2 \times 2 \times 2$ repetition of the cubic unit cell with randomly applied M- or R tilt modes and randomized MA orientations. Atomic positions and cell shapes were relaxed to a force threshold of 1×10^{-4} eV Å^{-1}. The relaxed structures were classified into phases by projecting onto the M and R modes using a mode projection tolerance of 0.2 Å. Figure 4.9 shows the resulting energy distributions, compared side-by-side with an equivalent analysis performed with a conventional NEP in [44].

Both models correctly identify the orthorhombic $a^-a^-c^+$ structure as the ground state. The energy distributions of the orthorhombic and tetragonal $a^0a^0c^-$ phases are qualitatively similar between the two models. However, the qNEP shows a higher relative occurrence of these crystalline phases compared to the conventional

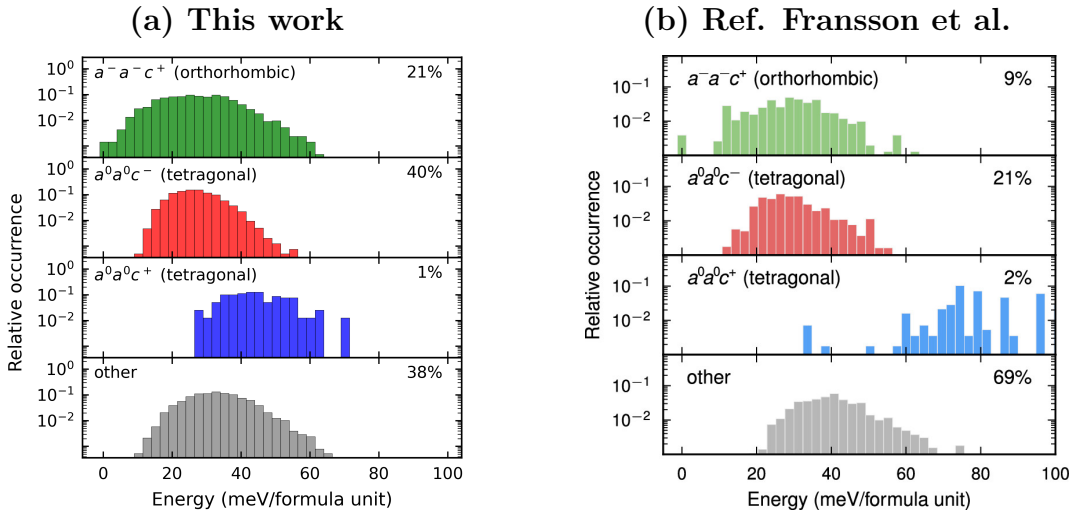

Figure 4.9: Energy distributions of 10 000 randomly oriented $MAPbI_3$ structures after structural relaxation. Panel (a) shows classifications using the qNEP potential in this work, while panel (b) reproduces results from a conventional NEP [44]. All energies are referenced to the lowest energy structure found.

NEP, with the tetragonal-orthorhombic ratio remaining approximately 2 in both cases. The tetragonal $a^0a^0c^+$ structure is rare for both potentials, but ends up at lower energies for the qNEP than for the NEP. Structures classified as "other" also appear at slightly lower energies than for the reference. A completely fair comparison is challenging due to potential differences in classification tolerances across the two models. The overall similarity in energy landscape suggests that the qNEP reproduces the thermodynamic ordering of $MAPbI_3$ reasonably well.

4.3 Response to a static electric field

This section presents the response of $MAPbI_3$ to a static electric field applied in the simulation Z-direction, corresponding to a pseudo-cubic face direction. The effect of the electric field on the phase behavior is first analyzed through field-temperature (E-T) phase diagrams, and cross-checked with isothermal field ramps. Subsequently, the origin of the field response is examined in terms of phonon mode projections and the orientational behavior of the MA cations, allowing the coupling between molecular dipoles and octahedral tilting to be characterized.

Figure 4.10 shows the resulting phase diagram, capturing all three phases of $MAPbI_3$. Since the cubic-to-tetragonal phase boundaries obtained from cooling runs differed only minimally from the heating results, only heating data are shown for clarity.

At low fields (here $\lesssim 0.015\,\mathrm{V/Å}$), the orthorhombic-to-tetragonal transition temperature increases slightly to 205 K while the tetragonal-cubic transition temperature remains unchanged at 360 K. At fields between $0.02\,\mathrm{V/Å}$ and $0.045\,\mathrm{V/Å}$, the orthorhombic-to-tetragonal transition temperature decreases rapidly, while the tetragonal-to-cubic transition shifts to higher temperatures. Above $0.045\,\mathrm{V/Å}$, the

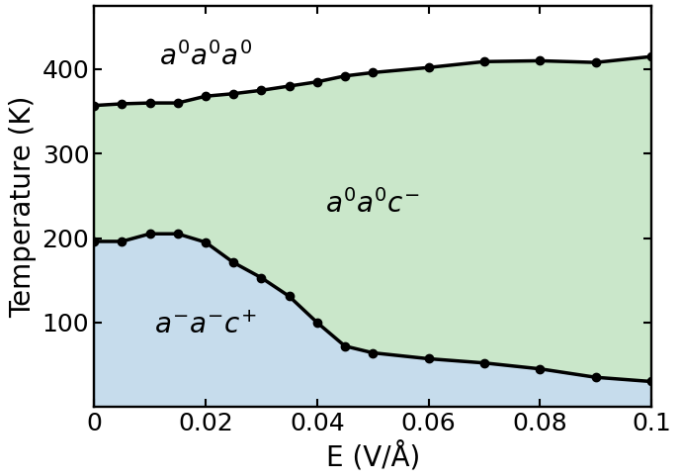

Figure 4.10: Field-temperature phase diagram for an electric field applied along a pseudo-cubic face. Glazer notation is used to label the phases: orthorhombic ($a^-a^-c^+$), tetragonal ($a^0a^0c^-$) and cubic ($a^0a^0a^0$).

response to the field begins to saturate. This is consistent with previous MD studies, where fields of order 0.01 V/Å were required to introduce sizable ordering of MA dipoles at room temperature [8].

Isothermal field sweeps were performed to cross-check the obtained phase diagram and characterize the field-induced structural response at fixed temperature. Starting from equilibrated configurations at zero field, the field strength was increased linearly to 0.1 V/Å at a rate of 0.02 V/Å/ns in the NPT ensemble. To check for hysteretic behavior, the field was subsequently reduced back to zero at the same rate. Phonon mode projections were extracted during the ramps to confirm the phase identity at each field strength. The potential energy during field ramps for temperatures that span all three phases is shown in Figure 4.11.

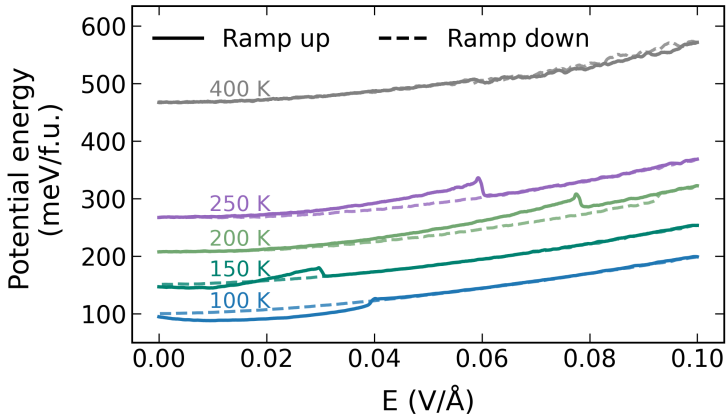

Figure 4.11: Potential energy per formula unit during isothermal field ramps with the harmonic thermal contribution ($1.5k_BT$) subtracted. The energy is referenced to the relaxed zero-field structure at 0 K. Each ramp begins from an equilibrated configuration without field, increases linearly to 0.1 V/Å, and returns to zero at the same rate (0.02 V/Å/ns).

All temperatures except 400 K show an abrupt jump in potential energy at specific field strengths. For 100 K and 150 K, the coercive fields of approximately 0.04 V/Å and 0.03 V/Å correspond to orthorhombic-to-tetragonal transitions, which matches with the boundary of the phase diagram. Some hysteresis is visible upon ramping back down, with higher energy reflecting the system remaining in the metastable tetragonal phase at low temperature. At 200 K and 250 K, the structure is practically in the tetragonal phase across all field strengths in the phase diagram. Yet both show an abrupt energy jump at high fields during the field ramp while remaining in the tetragonal phase. This represents a different type of reorientation, which is examined in the following part. No hysteresis is seen in this process: the energy returns to its initial energy. The orthorhombic-to-tetragonal transition at 205 K observed in low-field heating simulations is not visible in the 200 K isothermal ramp. This discrepancy likely reflects the system being trapped in a metastable state during heating at low fields, dependent on its initial conditions. At 400 K, transition to the tetragonal phase is visible near 0.06 V/Å, with the system reversibly returning to the cubic phase upon ramping back down.

Figure 4.12 shows the mode amplitudes (Q_M and Q_R) measured in the simulation coordinate system XYZ, during the electric field ramp for selected temperatures. This allowed analysis of field-induced structural reorientation. For clarity, only the non-zero components are shown.

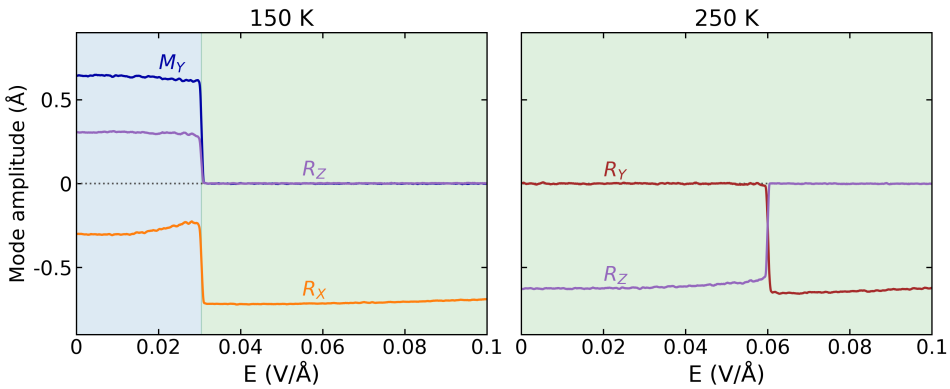

Figure 4.12: Evolution of mode amplitudes during a linear field-ramp from 0 to 0.1 V/Å, for 150 K and 250 K. The blue and green background regions indicate the orthorhombic and tetragonal phases, respectively. The mode components are expressed in the simulation coordinate system (X, Y, Z), with only the activated modes shown.

At 150 K, the system remains in the orthorhombic $a^-a^-c^+$ phase at low fields, where all three mode components are activated. Since the simulation coordinate system is used, the in-phase tilt about the c-axis is represented by an activation of M_Y. At about 0.03 V/Å, the transition to the tetragonal $a^0a^0c^+$ phase occurs, in which only a single R_X mode remains activated. This coercive field is consistent with the orthorhombic-to-tetragonal the phase boundary at 150 K in the E-T phase diagram. At 250 K, the system remains in the tetragonal phase across all fields strengths in the field ramp, consistent with the phase diagram. Initially, the R_Z mode is activated, which coincides with the field direction. At 0.06 V/Å, this

switches to an R_Y mode, reflecting a field-induced reorientation of the octahedral tilt axis perpendicular to the applied field. This reorientation occurs within the tetragonal phase and is therefore not captured by the E-T phase diagram. Heating simulations starting from low temperature show the same reorientation but at a significantly lower coercive field ($\sim 0.01\,\mathrm{V/Å}$), indicating that the transition is sensitive to thermal history. This suggests that the two tilt orientations are separated by an energy barrier under applied field. In total, the mode projections indicate that sufficiently strong electric fields favor structures in which the dominant octahedral tilt axis avoids alignment with the field direction.

Similarly to the zero-field case, the orientations of the $\boldsymbol{r}_{\mathrm{CN}}$ vectors were extracted to investigate the coupling between the PbI_6 octahedral framework and the MA cations. As the principal tilt axis reorients under the field, the crystal frame itself rotates relative to the simulation coordinates, so the field direction does not project onto a fixed crystallographic axis. The resulting distributions for two representative field strengths, a low field of $0.01\,\mathrm{V/Å}$ and an intermediate field of $0.03\,\mathrm{V/Å}$, are shown in Figure 4.13, for the same temperatures as in the zero-field case (150 K, 250 K, and 400 K).

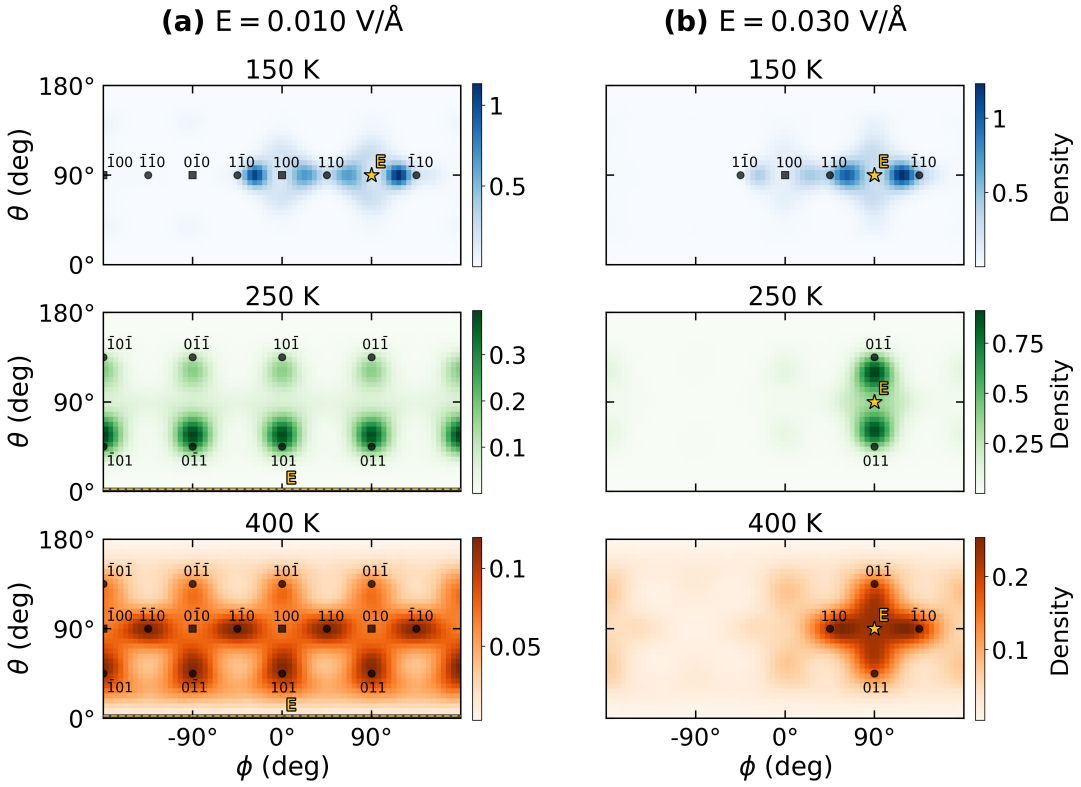

Figure 4.13: Distribution of the C−N bond vector in MA molecules for two representative field strengths, (a) 0.01 V/Å and (b) 0.03 V/Å, at three temperatures. Each panel uses independent probability density normalization. Crystallographic direction families ⟨110⟩ (circles) and ⟨100⟩ (squares) are indicated near regions of high probability density. The electric field direction (applied along simulation Z) is indicated by a horizontal dashed line at $\theta = 0°$ when aligned with the crystal [001] direction, or by a star when the octahedral tilt axis has reoriented under field, shifting the field direction to a different crystallographic axis.

For low field strengths, the orientational distributions remain qualitatively similar to those in Figure 4.6. Across all temperatures, an increase in intensity is observed for orientations closer to the field direction, reflecting partial dipole alignment. In the orthorhombic phase at 150 K, two of the zero-field orientations (near $\phi = -132°$ and $\phi = -42°$) vanish, while two new orientations appear, shifted toward the field direction. Yet significant density persists near the $[1\bar{1}0]$ and [100] points, which are directions anti-aligned or perpendicular to the field. This indicates competition between the applied field and the orthorhombic structural constraints: the field partially reorients some dipoles, while the tilt structure remains intact. At the higher field strength of 0.03 V/Å, these shifted orientations weaken, and those closest to the field direction dominate. Since this field strength coincides with the orthorhombic-to-tetragonal transition near 150 K, this evolution likely reflects the progressive destabilization of the orthorhombic phase. The preferred MA orientations in the orthorhombic structure are incompatible with alignment along the field direction. This concentration of density is coupled to the reorientation of the tilt axis away from the field direction: by tilting perpendicular to the field, the crystal

frame rotates such that the preferred ⟨110⟩ orientations of the tetragonal phase become compatible with alignment along the applied field. In the cubic phase at 400 K, the four orientations most compatible with the field direction become preferentially occupied. A substantial fraction of the density remains distributed over other orientations, reflecting the orientational disorder of the high-temperature phase. Notably, orientations antiparallel to the field remain suppressed.

To quantify the MA orientations efficiently across all field strengths, a global order parameter describing the net orientation of the MA molecules was defined as

$$\boldsymbol{N} = \frac{1}{N_{\mathrm{MA}}} \sum_i \hat{\mathbf{r}}_{\mathrm{CN},i}. \tag{4.2}$$

Here, N_{MA} is the number of MA molecules and $\hat{\mathbf{r}}_{\mathrm{CN},i}$ is the normalized C−N bond vector for molecule i, expressed in the crystal-aligned coordinate frame. The components N_x, N_y and N_z were extracted for different temperatures and electric field strengths during heating and cooling, shown in Figure 4.14.

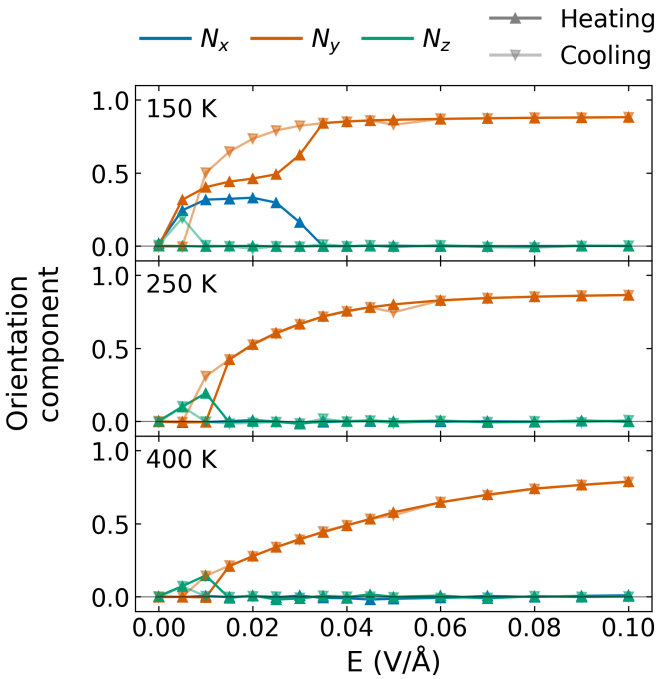

Figure 4.14: Components of the net MA orientation vector $\boldsymbol{N} = (N_x, N_y, N_z)$ extracted in the crystallographic frame. Data from heating (up triangles) and cooling (down triangles) are shown. For low fields (≤ 0.01 V/Å), the dominant octahedral tilt axis is aligned with the applied field direction, so the field direction corresponds to $N_z = 1$. Above this field strength, the field induces a reorientation of the tilt axis away from the field, causing the field direction to correspond to $N_y = 1$ in the crystal frame.

At zero field, the net orientation vanishes, $\boldsymbol{N} = \mathbf{0}$, for all temperatures, indicating that no preferred global molecular orientation is present. The distinction between low- and high-field behavior becomes particularly evident at 250 K, where the N_z

component initially increases with field strength. This represents the metastable region where the structure tilts along the same direction as the field. Above a critical field strength ($\gtrsim 0.01\,\mathrm{V/Å}$), the previously discussed structural reorientation occurs, accompanied by the onset of the N_y component for all temperatures. Following this reorientation, the electric field direction corresponds to $N_y = 1$, making the progressive alignment of the molecular dipoles with the field apparent.

The gradual destabilization of the orthorhombic phase is reflected in the onset of the N_x component at 150 K during heating, which corresponds to the two shifted orientations near $[1\bar{1}0]$ and [100] in Figure 4.13. This behavior likely reflects the competition between the orthorhombic ordering and field-induced dipole alignment, in which the orthorhombic cage constrains orientations that the field is trying to rotate away from. The absence of N_x during cooling, when the orthorhombic phase is skipped due to hysteresis, further confirms that this component reflects orthorhombic-phase behavior. An abrupt change occurs near $0.035\,\mathrm{V/Å}$, where N_x decreases toward zero while N_y increases to approximately 0.85. This marks the point at which the orthorhombic structure is no longer stable under the applied field. In the cubic phase, the magnitude of N_y remains smaller because thermal fluctuations allow the molecules to sample a broader range of orientations. The partial dipole alignment that nevertheless persists may contribute to the observed increase in the tetragonal-to-cubic transition temperature with increasing field strength.

To complete the structural analysis under applied fields, the Pb off-centering was analyzed during heating for six representative field strengths. Here, the components of $\langle \boldsymbol{d} \rangle$ were extracted in the simulation coordinate system with only the non-zero components $\langle d_X \rangle$ and $\langle d_Z \rangle$ shown in Figure 4.15.

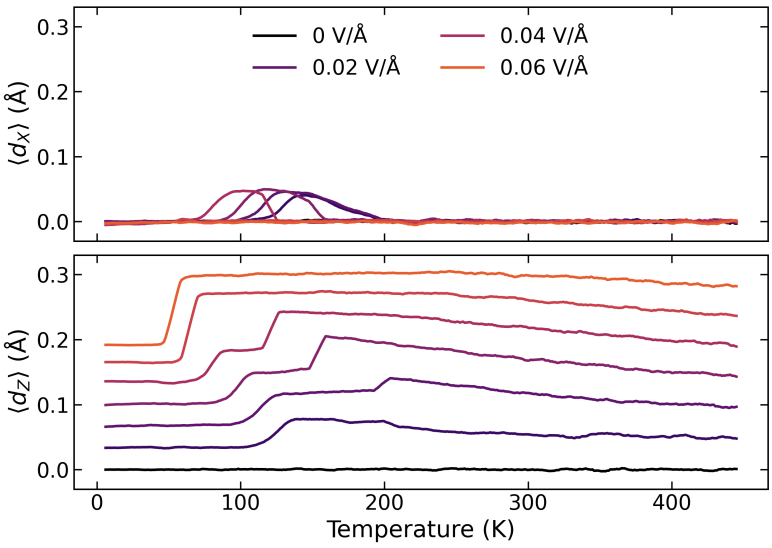

Figure 4.15: Pb off-centering in the X- and Z-direction for different field strengths. The field is applied in the Z-direction.

Without an applied electric field, the net Pb off-centering vanishes in all directions. For fields up to $0.04\,\mathrm{V/Å}$, a transient $\langle d_X \rangle$ appears at low temperatures, reaching a maximum of approximately 0.05 Å before vanishing at the orthorhombic-

to-tetragonal transition. At higher fields, $\langle d_X \rangle = 0$ everywhere. This transient behavior may be related to the competition between orthorhombic and field-induced ordering, previously observed as an onset of N_x in Figure 4.14. The Z-component is nonzero at all temperatures, with a magnitude that increases with field strength, reflecting a direct polar displacement of Pb along the field direction. At lower field strengths, the onset of $\langle d_X \rangle$ coincides with a step increase in $\langle d_Z \rangle$. This step sharpens further at the orthorhombic-to-tetragonal transition, where $\langle d_X \rangle$ vanishes. At higher fields this initial step is absent. Above the transition, $\langle d_Z \rangle$ decreases gradually with temperature, reflecting increasing thermal disorder.

4.3.1 Field-direction dependence

An electric field can be applied along seven distinct pseudo-cubic directions (without accounting for sign): [100], [010], [001], [110], [101], [011], and [111]. To explore anisotropic effects in $MAPbI_3$, two additional directions were considered: a $\langle 110 \rangle$-type direction applied along the XZ simulation axis, and the [111]-direction, which is orientation-independent in Cartesian coordinates. The field strength is defined as $E = \sqrt{E_X^2 + E_Y^2 + E_Z^2}$. For the XZ case, a field strength of $E = 0.03\,\mathrm{V/Å}$ corresponds to $E_X = E_Z = 0.03\,\mathrm{V/Å}/\sqrt{2}$.

Figure 4.16 shows the mode projections during heating and cooling for the two additional field directions at $0.03\,\mathrm{V/Å}$.

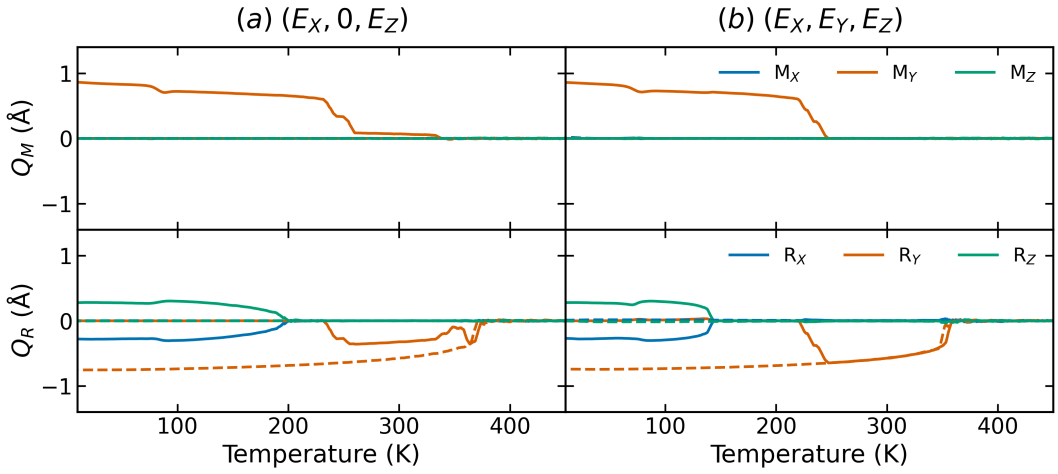

Figure 4.16: Mode projection amplitudes during heating (solid lines) and cooling (dashed lines) under an electric field of $0.03\,\mathrm{V/Å}$ applied in the (a) XZ-direction, and (b) XYZ-direction. In (a), a transition from the orthorhombic phase to a type of tetragonal phase occurs near 200 K, while in (b) the corresponding transition occurs near 140 K. Both systems transition to the cubic phase near 360 K.

For the XZ-directed field, the orthorhombic structure containing one M-mode and two R-modes persists up to approximately 195 K, identical to the transition temperature in the absence of an applied field. Notably, the initial structure had an R_X- and R_Z-mode, coinciding with the directions of the applied field. Between 200 K and 230 K, an intermediate tetragonal region appears in which the M_Y-mode is activated

instead of an R-mode. In Glazer notation, this corresponds to $a^0a^0c^+$ rather than the conventional tetragonal $a^0a^0c^-$ phase. However, it remains unclear whether this intermediate structure is a robust feature of the XZ-directed field or dependent on the initial configuration. Since the orthorhombic structure was initialized with its dominant tilt axis already aligned along the direction of no field ($E_Y = 0$) through the M_Y-mode, this may explain why the orthorhombic phase remains stabilized in this simulation. The tetragonal-to-cubic transition occurs near 360 K, again matching the zero-field case. Upon cooling, the system instead enters the conventional tetragonal phase with an activated R_Y-mode, consistent with the octahedral tilting occurring along the direction perpendicular to the field.

For the [111]-directed field, the orthorhombic-to-tetragonal transition is significantly suppressed to approximately 140 K, while the transition to the cubic phase remains near 360 K. The intermediate tetragonal region with in-phase tilting is correspondingly extended, although it terminates at approximately the same temperature, 230 K, as for the XZ-directed field. In this configuration, no tilt axis can develop perpendicular to the applied field, which likely contributes to the stronger suppression of the orthorhombic phase.

Finally, the distributions of MA orientations in the tetragonal phase were compared across the three field directions considered in this work, shown in Figure 4.17.

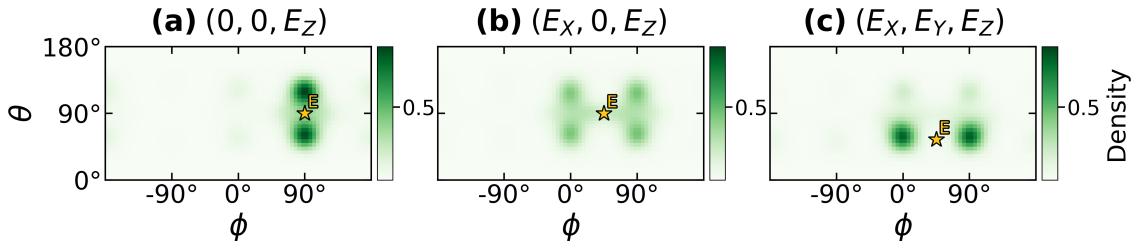

Figure 4.17: Distribution of MA orientations in the tetragonal phase at 250 K for a field directed in (a) Z-direction (b) XZ-direction (c) XYZ-direction, with field strength $E = 0.03\,\mathrm{V/Å}$. The MA orientations are expressed in the intrinsic crystallographic coordinate system and all distributions use the same normalization. The field directions are marked as a star.

Among the eight preferred MA orientations identified for the tetragonal phase in the absence of an external electric field, the preferred orientation landscape is preserved under applied field. However, the field biases the distribution toward orientations most closely aligned with its direction, without introducing new orientations. For both the ⟨100⟩-type and the [111] field directions, the applied field lies midway between two preferred MA orientations. In contrast, for the ⟨110⟩-type field, the field direction lies between four preferred orientations. Another thing to note is that there are traces of reorientation between the possible spots for the ⟨100⟩- and ⟨110⟩-types, while the same is not visible for the [111]-field.

4.4 Response to an oscillating electric field

In this section, the phase behavior of $MAPbI_3$ under an oscillating (AC) electric field is investigated. Frequency-temperature (f-T) phase diagrams were constructed for two field strengths (0.01 V/Å and 0.03 V/Å), revealing a significant suppression of the cubic-to-tetragonal transition across most frequencies. A localized resonant feature is observed, with the resonance frequency shifting from approximately 1.3 THz at the weaker field to 2.4 THz at the stronger field. To understand this resonance, several vibrational properties and spectra were studied in the absence of electric field: phonon dispersion, projected density of states (PDOS) and infrared (IR) activity. Its origin was further investigated through phonon mode projections of Γ-point modes under driven conditions.

4.4.1 Frequency-temperature phase diagrams

Figure 4.18 shows the f-T phase boundaries extracted from heating simulations, for an applied field $E(t) = E_0 \sin(2\pi f t)$ with $E_0 = 0.01$ V/Å and $E_0 = 0.03$ V/Å .

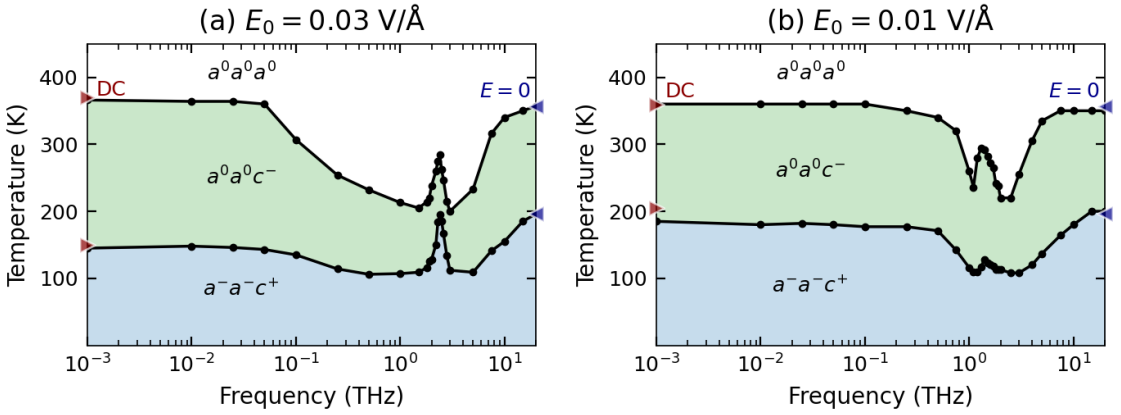

Figure 4.18: Frequency-temperature phase diagrams for (a) $E_0 = 0.03$ V/Å and (b) $E_0 = 0.01$ V/Å, applied in the simulation Z-direction. Corresponding transition temperatures for the static field (DC) and without field are marked for reference. The transition temperatures are suppressed for several frequencies, with a resonant peak near 2.4 THz for the higher field and 1.3 THz for the lower field, visible for both phase transitions.

For the stronger field, low frequencies ($\lesssim 0.05$ THz) show transition temperatures close to the static field values. For high frequencies ($\sim$ 20 THz), the transition temperatures approach their zero-field counterparts, though full convergence was not established within the simulated frequency range. In between these limits, the cubic-to-tetragonal transition is significantly suppressed, as is the tetragonal-to-orthorhombic transition. The strongest suppression occurs near $f = 1.5$ THz and $f = 2.8$ THz, where the cubic-to-tetragonal and tetragonal-to-orthorhombic transition temperatures reach approximately 200 K and 110 K, respectively. Between these two frequencies, however, both transition temperatures recover, reaching a

local maximum at 2.4 THz.

The weaker field exhibits qualitatively similar behavior, but with key quantitative differences. The onset of suppression is delayed to $\gtrsim 0.5$ THz and the resonant feature is shifted to lower frequency, with a local maximum at 1.3 THz. Additionally, the orthorhombic-to-tetragonal transition at low frequencies converges to approximately 185 K, about 20 K below the static field value. As discussed in Section 4.3, this discrepancy likely reflects metastability in the DC simulation, with the AC result potentially revealing the intrinsic phase behavior at this field strength.

A natural hypothesis regarding the phase behavior under an AC-field would be that the field directly drives the MA dipoles, disordering the orientations and destabilizing the low-temperature ordered phases. Since the reorientation timescale of MA in the cubic phase is on the order of 1 ps (corresponding to 1 THz), one might expect resonant coupling at this frequency. However, the observed resonant feature, where the low-temperature phases are locally more stabilized, suggests a more intricate picture. To investigate this, the vibrational spectrum and IR activity are examined in the following section.

4.4.2 Vibrational spectra

The phonon dispersion relates the vibrational frequency $\omega_\nu(\boldsymbol{q})$ to the wavevector $\boldsymbol{q}$, describing how phonons propagate through the crystal. The dispersion of $MAPbI_3$ in the cubic reference structure was computed within the harmonic approximation using `PHONOPY`. This was done with a $2 \times 2 \times 2$ supercell along the high-symmetry path

$$R\left[\tfrac{1}{2},\tfrac{1}{2},\tfrac{1}{2}\right] \to \Gamma\,[0,0,0] \to M\left[\tfrac{1}{2},\tfrac{1}{2},0\right] \to X\left[\tfrac{1}{2},0,0\right],$$

where coordinates are given in units of the reciprocal lattice vectors. Throughout this section, vibrational frequencies are expressed as ordinary frequency $f_\nu(\boldsymbol{q}) = \omega_\nu(\boldsymbol{q})/2\pi$ in THz, allowing direct comparison with the driving frequency f of the oscillating field. The resulting dispersion is shown in Figure 4.19.

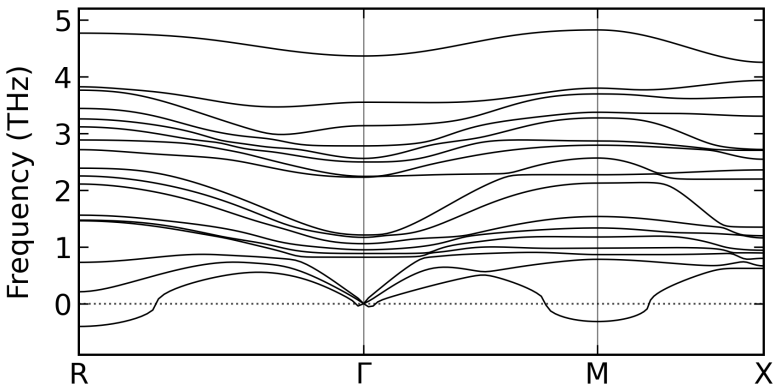

Figure 4.19: Phonon dispersion for the cubic structure displayed for frequencies up to 5 THz. Imaginary modes are visualized as negative frequencies.

Imaginary modes are visible at the M and R zone boundaries, reflecting the familiar octahedral tilting instability of the cubic reference structure that drives the

transition to the tetragonal and orthorhombic phases. As discussed in Section 2.1, only zone-center ($\boldsymbol{q} = 0$) modes can couple directly to a spatially uniform oscillating electric field. Two Γ-point modes are found in close proximity near 2.3 THz, any of which could in principle be responsible for the resonant feature observed in the $E_0 = 0.03\,\mathrm{V/Å}$ f-T phase diagram, provided they are IR-active. Likewise, several Γ-point modes are present near 1.3 THz, matching the resonant feature observed in the $E_0 = 0.01\,\mathrm{V/Å}$ diagram. However, since the dispersion was computed within the harmonic approximation for the cubic structure, the resulting frequencies should be treated as indicative only, as anharmonic effects can shift mode frequencies significantly.

To gain further insight into the character of the vibrational modes at several temperatures, the density of states (DOS) was computed during MD simulations using `gpumd` functionality, for the full simulation cell of 32928 atoms. Heating to the target temperature was done in the NPT ensemble, followed by an equilibration of 1 ns in the NVT ensemble and finally production runs in the NVE ensemble for 400 ps. The total DOS for different temperatures are shown in Figure 4.20.

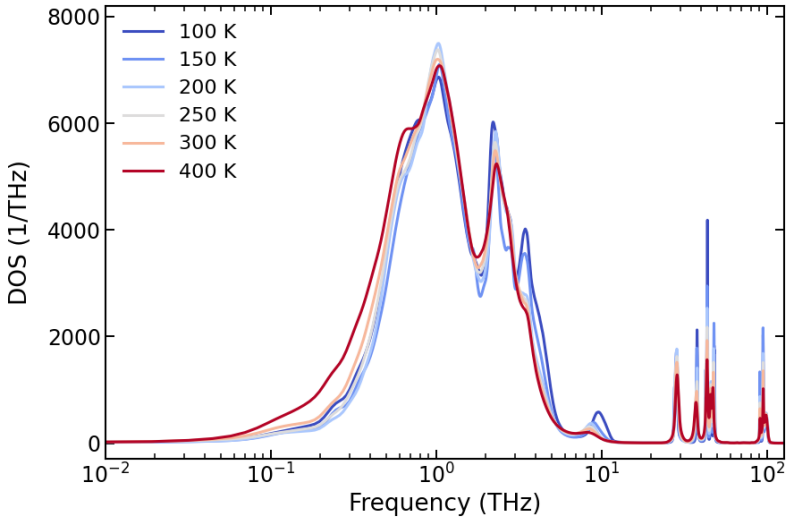

Figure 4.20: Total density of states at multiple temperatures. The spectrum extends to approximately 100 THz, showing the full range of vibrational modes in $MAPbI_3$.

The qualitative behavior of the DOS is similar across all temperatures, with two prominent peaks near 1 THz and 2.4 THz, and further near 3.5 THz and 10 THz. The spectrum is flat at frequencies below 0.05 THz, consistent with the low-frequency convergence to the static field in the f-T diagram. Similarly, there is a flat region between 10 THz and 25 THz, which coincides with the high-frequency plateau in the diagram. Furthermore, several peaks exist at higher frequencies outside of the range for the AC-field simulations. To identify the origin of the dominant peaks near 1 THz and 2.4 THz, a species-resolved PDOS was computed for each atom type. Since the spectral features are representative across all relevant temperatures, the PDOS is shown only for 200 K in Figure 4.21.

Modes up to approximately 5 THz are dominated by I and Pb vibrations, con-

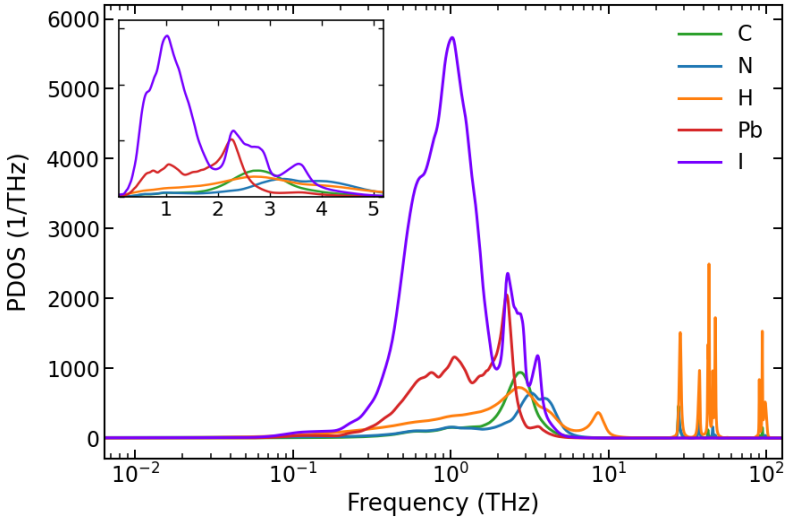

Figure 4.21: Projected density of states per atom species at 200 K. The inset shows the spectrum up to 5 THz in linear x-scale, relevant for the resonant region in the f-T diagram.

sistent with vibrations of the PbI_6 framework. In particular, the peaks near 1 THz and 2.4 THz arise mainly from Pb and I motion, with smaller contributions from the MA species. Above 7 THz, the vibrational spectrum is dominated exclusively by MA modes. These results can be compared with DFT studies of the orthorhombic phase, which attributed the low-frequency modes between approximately 0.7 and 1.5 THz to various Pb–I–Pb rocking and bending motions. Modes in the range 1.6–3.2 THz have been associated with Pb–I–Pb stretching vibrations, with one bending mode at 2.4 THz. MA librational and translational motions occur primarily between 1.8 and 5.4 THz, while higher-frequency modes (24–93 THz) correspond to internal MA vibrations, such as bond stretching [49].

While this identifies which atoms move at each frequency, it does not directly reveal which modes couple strongly to the electric field. To identify IR-active (Γ) modes, a qualitative IR spectrum was computed as the power spectral density (PSD) of the polarization current autocorrelation function, according to Equation (2.17). This was done from trajectories in the NVE ensemble at 200 K, with the resulting spectrum shown in Figure 4.22.

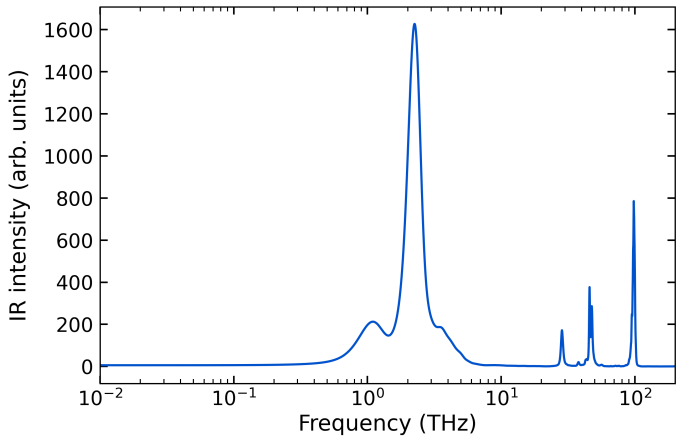

Figure 4.22: IR spectrum computed as the PSD of $\dot{\mathbf{P}}(t)$ at 200 K. A dominant peak near 2.4 THz is observed.

The peak near 2.4 THz dominates the IR spectrum, indicating that Γ-modes with this frequency can couple strongly to an external field. The onset and end of this peak is at approximately 1.5 and 2.8 THz, respectively, which matches the region of the resonant feature in the $E_0 = 0.03\,\mathrm{V/Å}$ f-T diagram. There is also a smaller feature near 1 THz, which is closer to the shifted resonance peak at the lower field strength. To resolve which atoms drive this coupling, an IR spectrum per species was constructed by considering the polarization current $\dot{\boldsymbol{P}}_s(t) = \sum_{i \in s} Z_i^* \boldsymbol{v}_i(t)$ for each species s, shown in Figure 4.23.

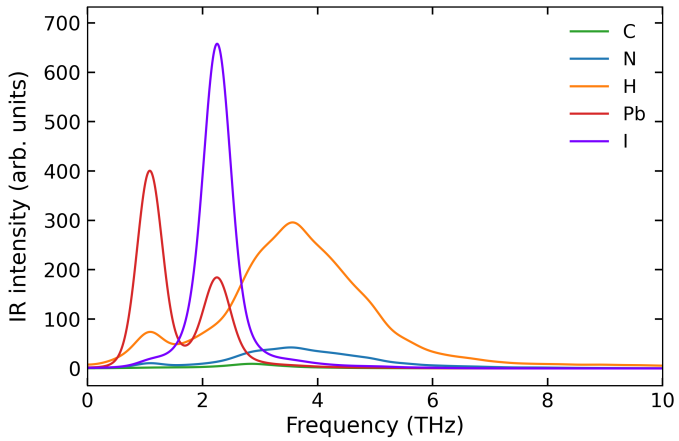

Figure 4.23: IR spectrum resolved by atom species at 200 K, focused on the low frequency region.

IR activity near 2.4 THz is dominated by iodine motion. According to the DFT assignments discussed previously, this feature could correspond to a Pb–I–Pb bending or stretching mode. For the weaker field strength, the resonant feature shifts to 1.3 THz, where the IR activity is comparatively weak, with contributions primarily from Pb and H and no distinct iodine peak.

To analyze excitation of specific modes, the Γ-point phonon modes were projected onto MD trajectories with and without applied AC-fields. The mode eigenvectors

were obtained with the same methodology used for the phonon dispersion calculation. This was done for the 0.03 V/Å field strength at three frequencies: below the resonant peak (1 THz), at the maximum of the peak (2.4 THz) and above the peak (3 THz) in the NVT ensemble. Several eigenmodes with vibrational frequencies near 1 THz and 2.3 THz showed coherence to the field, two of which are displayed in Figure 4.24.

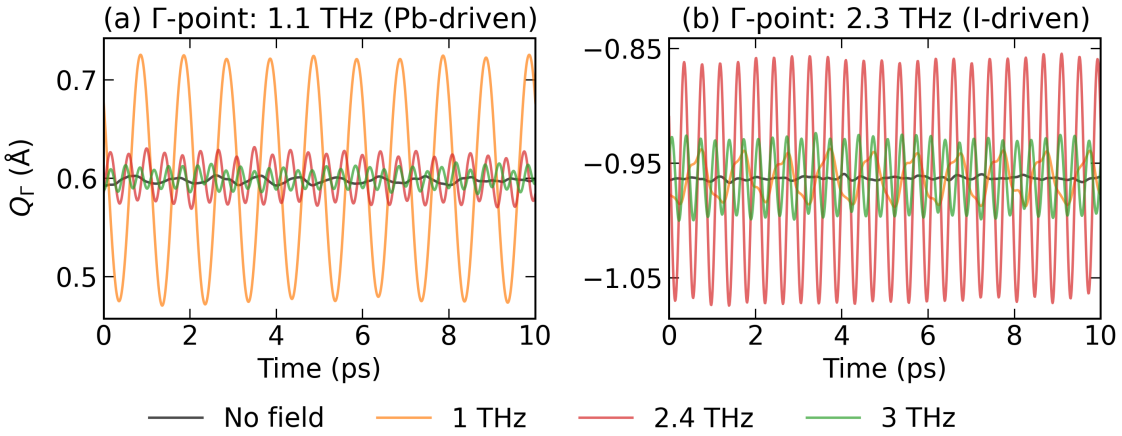

Figure 4.24: Evolution of (a) a Γ-point mode dominated by Pb motion and (b) a Γ-point mode dominated by I motion, with and without an applied AC-field ($E_0 = 0.03\,\mathrm{V/Å}$). Clear coherence is seen when the Pb mode is driven at 1 THz and when the I mode is driven at 2.4 THz.

The Γ-point mode at 1.1 THz, identified with Pb-motion, shows strong coherence when driven at 1 THz. Similarly, the Γ-point mode at 2.3 THz identified with I-motion responds strongly to a field at 2.4 THz. For both cases, the other driving frequencies that are not resonant with the mode still show more activation than at zero field. The persistence of coherence despite the approximate nature of the eigenvectors suggests the resonant coupling is a robust feature of the system dynamics.

Modes at other high-symmetry points were also checked to confirm that the Γ-point modes are the main contributors. For demonstration, two modes at the X-point, which had approximately the same frequencies (1.1 THz and 2.3 THz) were projected from the trajectories, shown in Figure 4.25.

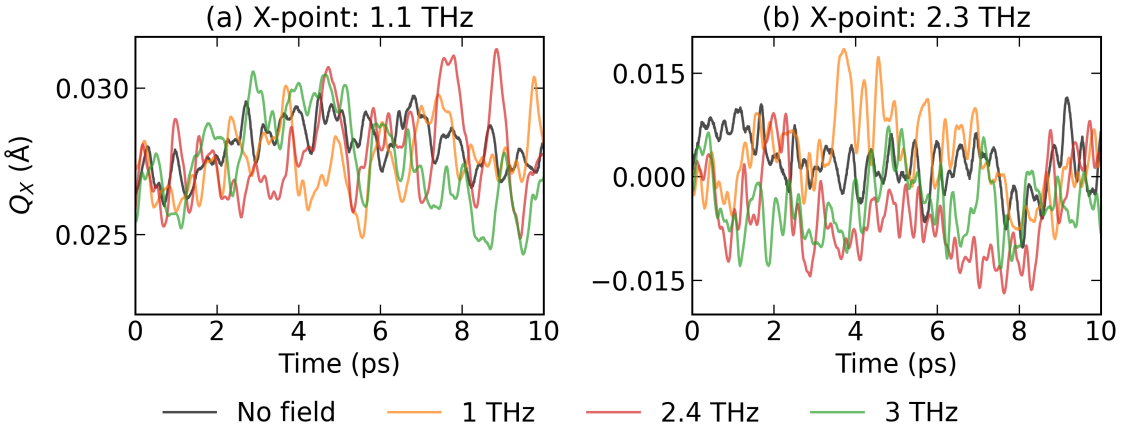

Figure 4.25: Evolution of X-point modes at (a) 1.1 THz and (b) 2.3 THz, with and without an applied AC-field. All amplitudes are small, $|Q_X| \lesssim 0.03$ Å, and show no particular coherence.

To examine how the excited Γ-modes influence MA dynamics, the orientational ACF was computed under applied AC fields for temperatures between 150 K and 350 K in the NVT ensemble. For each field strength, simulations were performed both below resonance (1 THz) and near the resonant feature (1.3 THz and 2.4 THz), with the resulting rotational correlation times summarized in Table 4.1.

Table 4.1: Rotational correlation times τ_{rot} (ps) for MA cations under oscillating electric fields at frequencies below and near resonant regions. Cell background colors indicate the phase: blue for orthorhombic, green for tetragonal and orange for cubic. The rotation times without field are included for reference.

Temperature (K)	$E = 0$	$E_0 = 0.01$		$E_0 = 0.03$	
		1 THz	1.3 THz	1 THz	2.4 THz
150	>200	12	14	6.9	38
200	29	4.5	7.7	2.4	3.8
250	8.0	2.4	3.4	1.2	1.5
300	3.0	1.3	1.7	0.73	0.85
350	1.5	0.85	0.96	0.54	0.55
400	0.92	—	—	—	—

Across all frequencies, the rotational correlation time decreases relative to the zero-field case, indicating that the applied AC field generally accelerates MA reorientation. This is consistent with the reduced transition temperatures observed in the phase diagrams under applied fields. An exception occurs for the orthorhombic-to-tetragonal transition at $E_0 = 0.03$ V/Å and 2.4 THz, where the transition temperature remains approximately unchanged from the zero-field value (195 K). Although the rotational correlation time at 2.4 THz is still lower than in the absence of a field, it is significantly larger than at 1 THz at 150 K. Together with the strong

iodine-dominated IR activity near 2.4 THz, this supports the interpretation that a resonantly driven Pb−I framework mode partially suppresses MA reorientation. A similar trend is observed for the lower field strength: near the resonant feature at 1.3 THz, the MA rotational correlation times are slightly larger than at 1 THz. Once the system enters the cubic phase, the MA molecules rotate more freely, consistent with the larger and more symmetric cavity of the high-temperature structure.

Since the vibrational spectrum itself is relatively temperature-independent, one might expect both field strengths to resonate at the same frequencies. However, the resonance behavior likely depends not only on the phonon spectrum, but also on the temperature-dependent coupling between framework distortions and MA orientational dynamics. Outside the resonant regions, below 1 THz and above 3 THz, the iodine contribution to the IR spectrum becomes much weaker, while Pb and H contributions dominate. In these frequency ranges, where the cubic phase remains stable down to remarkably low temperatures, the stabilization mechanism may therefore be more strongly connected to MA reorientational dynamics than to resonantly driven framework vibrations.

5

Conclusion

This work investigated the structural response of $MAPbI_3$ to static and oscillating electric fields using MD simulation with a qNEP model. The study systematically characterized field-induced changes in phase behavior, octahedral tilting, MA cation orientations, and vibrational properties across a range of field strengths and frequencies. The qNEP model used in this work achieves high accuracy in reproducing DFT reference calculations ($R^2 \geq 0.985$). The energy distribution analysis of 10 000 randomly initialized structures confirmed that the qNEP model reproduces the thermodynamic ordering of $MAPbI_3$ phases reasonably well, with 61% of structures classified into recognized phases.

In the absence of external fields, $MAPbI_3$ exhibits the well-known orthorhombic-to-tetragonal-to-cubic phase sequence upon heating, with transition temperatures approximately 30 K higher than experiment. This discrepancy, while notable, is within the normal range of machine-learned potential MD studies and does not qualitatively affect the conclusions. Upon cooling, only the cubic-to-tetragonal transition occurs, supporting the first-order character of the tetragonal-to-orthorhombic transition. The MA molecules are initialized in an ordered, near-static, configuration in the orthorhombic phase and progressively sample a larger set of orientations as temperature increases.

Under static electric fields, the phase boundaries are shifted significantly: the orthorhombic-to-tetragonal transition is suppressed by up to 150 K, while the tetragonal-to-cubic transition is raised by up to 40 K. A key finding is that the octahedral tilt axis in the tetragonal structure reorients away from the applied field direction under sufficiently high field strengths. This reorientation enables the preferred $\langle 110 \rangle$ MA orientations to align with the field while remaining compatible with the tetragonal cage geometry. The critical field strength for this reorientation depends on thermal history, suggesting that the two tilt orientations are separated by an energy barrier under applied field. MA dipoles show progressive alignment with the field direction, reaching approximately 85% alignment in the tetragonal phase. The orientational preferences of MA molecules in the orthorhombic phase are incompatible with alignment along the applied field direction, likely contributing to the destabilization of this phase. For the other field directions briefly explored here (one $\langle 110 \rangle$-type and [111]), the same general behavior of octahedral tilt reorientation and MA alignment was observed.

The response to oscillating electric fields revealed a more complex mechanism than simple dipole disordering. Under oscillating electric fields, both transition temperatures are generally suppressed across most frequencies, consistent with molecular dipoles responding to the time-varying field. However, localized resonant features

emerge in the frequency-temperature phase diagrams at 1.3 THz ($E_0 = 0.01\,\mathrm{V/Å}$) and 2.4 THz ($E_0 = 0.03\,\mathrm{V/Å}$). These resonances correspond to IR-active PbI_6 framework vibrations, with the lower-frequency resonance dominated by Pb and H contributions and the higher-frequency resonance dominated by Pb and I motion. At these resonant frequencies, the driven framework modes partially suppress MA cation reorientation, locally stabilizing low-symmetry phases. This interpretation is supported more strongly by the results at higher field strength, where the resonant feature is more pronounced.

The collective findings of this study highlight the complex interplay between three key components: the MA molecular dipoles, the inorganic PbI_6 framework, and the external electric field. In static fields, the coupling is relatively direct: the field polarizes and reorients MA dipoles, which destabilize ordered phases by frustrating the interactions that normally stabilize them. In oscillating fields, the situation is more subtle. Rather than directly driving molecular reorientation, certain frequencies resonantly excite collective framework vibrations that, paradoxically, partially suppress reorientation and stabilize lower-temperature phases. This demonstrates that understanding field-driven structural changes requires considering how external perturbations couple to both individual molecular degrees of freedom and collective lattice modes.

In conclusion, these results demonstrate that external electric fields can strongly and nontrivially modify phase stability in hybrid perovskites, with responses that depend sensitively on both temperature, field strength and frequency. Future work should extend these investigations in several directions. Simulations at lower field strengths, approaching realistic experimental ranges, would clarify the quantitative applicability of the findings. Systematic exploration of fields applied to all seven pseudo-cubic directions would provide a complete picture of anisotropic effects and test whether the resonant stabilization mechanism is direction-dependent. Given the different resonance frequencies for the two field strengths, it would be instructive to map out the dependence of resonance frequency as a function of field strength.

Bibliography

[1] Lioz Etgar. "Hybrid Perovskites beyond Photovoltaics: Unlocking Multifunctional Energy and Optoelectronic Applications". In: *ACS Energy Letters* 11.1 (2026), pp. 161–171. DOI: 10.1021/acsenergylett.5c03409.

[2] Kacper Drużbicki et al. "Cation Dynamics and Structural Stabilization in Formamidinium Lead Iodide Perovskites". In: *The Journal of Physical Chemistry Letters* 12.14 (2021). PMID: 33792334, pp. 3503–3508. DOI: 10.1021/acs.jpclett.1c00616.

[3] Jung-Hoon Lee et al. "Resolving the Physical Origin of Octahedral Tilting in Halide Perovskites". In: *Chemistry of Materials* 28.12 (2016), pp. 4259–4266. DOI: 10.1021/acs.chemmater.6b00968.

[4] A. Poglitsch and D. Weber. "Dynamic disorder in methylammoniumtrihalogenoplumbates (II) observed by millimeter-wave spectroscopy". In: *Journal of Chemical Physics* 87.11 (1987), pp. 6373–6378.

[5] Tianran Chen et al. "Rotational dynamics of organic cations in the CH3NH3PbI3 perovskite". In: *Phys. Chem. Chem. Phys.* 17 (46 2015), pp. 31278–31286. DOI: 10.1039/C5CP05348J.

[6] Alexander N. Beecher et al. "Direct Observation of Dynamic Symmetry Breaking above Room Temperature in Methylammonium Lead Iodide Perovskite". In: *ACS Energy Letters* 1.4 (2016), pp. 880–887. DOI: 10.1021/acsenergylett.6b00381.

[7] Lucy D. Whalley et al. "Phonon anharmonicity, lifetimes, and thermal transport in $CH_3NH_3PbI_3$ from many-body perturbation theory". In: *Physical Review B* 94.22 (2016), 220301(R). DOI: 10.1103/PhysRevB.94.220301.

[8] Shi Liu and R. E. Cohen. "Response of Methylammonium Lead Iodide to External Stimuli and Caloric Effects from Molecular Dynamics Simulations". In: *The Journal of Physical Chemistry C* 120.31 (2016), pp. 17274–17281. DOI: 10.1021/acs.jpcc.6b06416.

[9] Heejae Kim et al. "Direct Observation of Mode-Specific Phonon-Band Gap Coupling in Methylammonium Lead Halide Perovskites". In: *Nature Communications* 8 (2017), p. 687. DOI: 10.1038/s41467-017-00807-x.

[10] Keke Song et al. "General-purpose machine-learned potential for 16 elemental metals and their alloys". In: *Nature Communications* 15 (2024), p. 10208. DOI: 10.1038/s41467-024-54554-x.

[11] Michael P. Marder. *Condensed Matter Physics*. 2nd ed. Wiley, 2010.

[12] Xavier Gonze and Changyol Lee. "Dynamical matrices, Born effective charges, dielectric permittivity tensors, and interatomic force constants from density-

functional perturbation theory". In: *Physical Review B* 55.16 (1997), pp. 10355–10368. DOI: 10.1103/PhysRevB.55.10355.

[13] P. Umari and Alfredo Pasquarello. "Ab initio Molecular Dynamics in a Finite Homogeneous Electric Field". In: *Physical Review Letters* 89.15 (2002), p. 157602. DOI: 10.1103/PhysRevLett.89.157602.

[14] P. Umari and Alfredo Pasquarello. "Infrared and Raman spectra of disordered materials from first principles". In: *Diamond and Related Materials* 14 (2005), pp. 1255–1261. DOI: 10.1016/j.diamond.2004.12.007.

[15] Bernhard Schmiedmayer and Georg Kresse. "Derivative learning of tensorial quantities – Predicting finite temperature infrared spectra from first principles". In: (2024). arXiv: 2404.19674 [cond-mat.mtrl-sci].

[16] L. D. Landau and E. M. Lifshitz. *Statistical Physics, Part 1*. Pergamon Press, 1980.

[17] Quinten A. Akkerman and Liberato Manna. "What Defines a Halide Perovskite?" In: *ACS Energy Letters* 5.2 (2020). PMID: 33344766, pp. 604–610. DOI: 10.1021/acsenergylett.0c00039.

[18] Joshua Young and James M. Rondinelli. "Octahedral Rotation Preferences in Perovskite Iodides and Bromides". In: *The Journal of Physical Chemistry Letters* 7.5 (2016). PMID: 26899936, pp. 918–922. DOI: 10.1021/acs.jpclett.6b00094.

[19] A. M. Glazer. "The Classification of Tilted Octahedra in Perovskites". In: *Acta Crystallographica Section B* 28 (1972), pp. 3384–3392. DOI: 10.1107/S0567740872007976.

[20] Harold T. Stokes et al. "Group-theoretical analysis of octahedral tilting in ferroelectric perovskites". In: *Acta Crystallographica Section B* 58 (2002), pp. 934–938. DOI: 10.1107/S0108768102012025.

[21] Zhen Li et al. "Stabilizing Perovskite Structures by Tuning Tolerance Factor: Formation of Formamidinium and Cesium Lead Iodide Solid-State Alloys". In: *Chemistry of Materials* 28.1 (2016), pp. 284–292. DOI: 10.1021/acs.chemmater.5b04107.

[22] Sudeep Maheshwari et al. "The Relation between Rotational Dynamics of the Organic Cation and Phase Transitions in Hybrid Halide Perovskites". In: *The Journal of Physical Chemistry C* 123.23 (2019). PMID: 31258830, pp. 14652–14661. DOI: 10.1021/acs.jpcc.9b02736.

[23] Daan Frenkel and Berend Smit. *Understanding Molecular Simulation: From Algorithms to Applications*. 2nd ed. San Diego: Academic Press, 2002. ISBN: 978-0-12-267351-1.

[24] H. J. C. Berendsen et al. "Molecular dynamics with coupling to an external bath". In: *The Journal of Chemical Physics* 81.8 (1984), pp. 3684–3690. DOI: 10.1063/1.448118.

[25] Mark E. Tuckerman. *Statistical Mechanics: Theory and Molecular Simulation*. Oxford University Press, 2010.

[26] Mattia Bernetti and Giovanni Bussi. "Pressure control using stochastic cell rescaling". In: *The Journal of Chemical Physics* 153.11 (2020), p. 114107. DOI: 10.1063/5.0020514.

[27] Robert G. Parr and Weitao Yang. *Density-Functional Theory of Atoms and Molecules*. Oxford University Press, 1994.

[28] P. Hohenberg and W. Kohn. "Inhomogeneous Electron Gas". In: *Physical Review* 136.3B (1964), B864–B871. DOI: 10.1103/PhysRev.136.B864.

[29] W. Kohn and L. J. Sham. "Self-Consistent Equations Including Exchange and Correlation Effects". In: *Physical Review* 140.4A (1965), A1133–A1138. DOI: 10.1103/PhysRev.140.A1133.

[30] Tom Schaul, Tobias Glasmachers, and Jürgen Schmidhuber. "High Dimensions and Heavy Tails for Natural Evolution Strategies". In: *Proceedings of the 13th Annual Conference on Genetic and Evolutionary Computation*. GECCO '11. Dublin, Ireland: Association for Computing Machinery, 2011, pp. 845–852. ISBN: 9781450305570. DOI: 10.1145/2001576.2001692.

[31] Zheyong Fan et al. "Neuroevolution machine learning potentials: Combining high accuracy and low cost in atomistic simulations and application to heat transport". In: *Physical Review B* 104.10 (2021), p. 104309.

[32] Zheyong Fan et al. "qNEP: A highly efficient neuroevolution potential with dynamic charges for large-scale atomistic simulations". In: *Journal of Chemical Theory and Computation* 22 (2026), p. 4787. DOI: 10.1021/acs.jctc.6c00146.

[33] Ask Hjorth Larsen et al. "The atomic simulation environment—a Python library for working with atoms". In: *Journal of Physics: Condensed Matter* 29.27 (2017), p. 273002. DOI: 10.1088/1361-648X/aa680e.

[34] Eric Lindgren et al. "calorine: A Python package for constructing and sampling neuroevolution potential models". In: *Journal of Open Source Software* 9 (2024), p. 6264. DOI: 10.21105/joss.06264.

[35] Erik Fransson et al. "dynasor—A Tool for Extracting Dynamical Structure Factors and Current Correlation Functions from Molecular Dynamics Simulations". In: *Advanced Theory and Simulations* 4.2 (2021), p. 2000240. DOI: 10.1002/adts.202000240.

[36] Esmée Berger et al. "Dynasor 2: From simulation to experiment through correlation functions". In: *Computer Physics Communications* 316 (2025), p. 109759. DOI: 10.1016/j.cpc.2025.109759.

[37] Fredrik Eriksson, Erik Fransson, and Paul Erhart. "The Hiphive Package for the Extraction of High-Order Force Constants by Machine Learning". In: *Advanced Theory and Simulations* 2.5 (2019), p. 1800184. DOI: 10.1002/adts.201800184.

[38] Alexander Stukowski. "Visualization and analysis of atomistic simulation data with OVITO—the Open Visualization Tool". In: *Modelling and Simulation in Materials Science and Engineering* 18.1 (2009), p. 015012. DOI: 10.1088/0965-0393/18/1/015012.

[39] Julia Wiktor et al. "Quantifying Dynamic Tilting in Halide Perovskites: Chemical Trends and Local Correlations". In: *Chemistry of Materials* 35.17 (2023), pp. 6737–6744. DOI: 10.1021/acs.chemmater.3c00933.

[40] Pauli Virtanen et al. "SciPy 1.0: Fundamental Algorithms for Scientific Computing in Python". In: *Nature Methods* 17.3 (2020), pp. 261–272. DOI: 10.1038/s41592-019-0686-2.

[41] Tao Sun, Xiao Shen, and Philip B. Allen. "Phonon quasiparticles and anharmonic perturbation theory tested by molecular dynamics on a model system". In: *Physical Review B* 82.22 (2010), p. 224304. DOI: 10.1103/PhysRevB.82.224304.

[42] Atsushi Togo et al. "Implementation strategies in phonopy and phono3py". In: *Journal of Physics: Condensed Matter* 35.35 (2023), p. 353001. DOI: 10.1088/1361-648X/acd831.

[43] Nripen Besra, Supratim Maity, and Kalyan Kumar Chattopadhyay. "Photo tuned electron field emission from vertically aligned $CH_3NH_3PbI_3$ nanorods grown in AAO template". In: *Journal of Physics and Chemistry of Solids* 161 (2022), p. 110457. DOI: 10.1016/j.jpcs.2021.110457.

[44] Erik Fransson et al. "Revealing the Free Energy Landscape of Halide Perovskites: Metastability and Transition Characters in $CsPbBr_3$ and $MAPbI_3$". In: *Chemistry of Materials* 35.19 (2023), pp. 8229–8238. DOI: 10.1021/acs.chemmater.3c01740.

[45] T. Hainer et al. "A morphotropic phase boundary in $MA_{1-x}FA_xPbI_3$: linking structure, dynamics, and electronic properties". In: *Nature Communications* 16 (2025), p. 8775. DOI: 10.1038/s41467-025-64526-4.

[46] P. S. Whitfield et al. "Structures, Phase Transitions and Tricritical Behavior of the Hybrid Perovskite Methyl Ammonium Lead Iodide". In: *Scientific Reports* 6.1 (2016). Published 21 October 2016, p. 35685. DOI: 10.1038/srep35685.

[47] A. Mattoni et al. "Methylammonium Rotational Dynamics in Lead Halide Perovskite by Classical Molecular Dynamics: The Role of Temperature". In: *The Journal of Physical Chemistry C* 119.30 (2015), pp. 17421–17428. DOI: 10.1021/acs.jpcc.5b04283.

[48] Kohei Shimamura et al. "Rotation mechanism of methylammonium molecules in organometal halide perovskite in cubic phase: An ab initio molecular dynamics study". In: *The Journal of Chemical Physics* 145.22 (2016), p. 224503. DOI: 10.1063/1.4971791.

[49] Miguel Osorio et al. "Vibrational Properties of the Organic-Inorganic Halide Perovskite $CH_3NH_3PbI_3$ from Theory and Experiment: Factor Group Analysis, First-Principles Calculations, and Low-Temperature Infrared Spectra". In: *The Journal of Physical Chemistry C* 119 (2015). DOI: 10.1021/acs.jpcc.5b07432.

DEPARTMENT OF PHYSICS
CHALMERS UNIVERSITY OF TECHNOLOGY
Gothenburg, Sweden
www.chalmers.se

CHALMERS
UNIVERSITY OF TECHNOLOGY